

MDPI

Article

Jet in Accelerating Turbulent Crossflow with Passive Scalar Transport [†]

Carlos Quiñones and Guillermo Araya *

HPC and Visualization Laboratory, Department of Mechanical Engineering, University of Puerto Rico at Mayaguez, Mayaguez, PR 00681, USA; carlos.quinones1@upr.edu

- * Correspondence: araya@mailaps.org
- † This paper is an extended version of our paper published in ASME 2017 International Mechanical Engineering Congress and Exposition, Tampa, FL, USA, 3–9 November 2017.

Abstract: The interaction of a turbulent, spatially developing crossflow with a transverse jet possesses several engineering and technological applications such as film cooling of turbine blades, exhaust plumes, thrust vector control, fuel injection, etc. Direct Numerical Simulation (DNS) of a jet in a crossflow under different streamwise pressure gradients (zero and favorable pressure gradient) is carried out. The purpose is to study the physics behind the transport phenomena and coherent structure dynamics in turbulent crossflow jets at different streamwise pressure gradients and low/high-velocity ratios (0.5 and 1). The temperature was regarded as a passive scalar with a molecular Prandtl number of 0.71. The analysis is performed by prescribing accurate turbulent information (instantaneous velocity and temperature) at the inlet of a computational domain. The upward motion of low-momentum fluid created by the "legs" of the counter-rotating vortex pair (CVP) encounters the downward inviscid flow coming from outside of the turbulent boundary layer, inducing a stagnation point and a shear layer. This layer is characterized by high levels of turbulent mixing, turbulence production, turbulent kinetic energy (TKE) and thermal fluctuations. The formation and development of the above-mentioned shear layer are more evident at higher velocity ratios.

Keywords: DNS; crossflow jet; turbulent boundary layer; passive scalar



Citation: Quiñones, C.; Araya, G. Jet in Accelerating Turbulent Crossflow with Passive Scalar Transport. *Energies* **2022**, *15*, 4296. https:// doi.org/10.3390/en15124296

Academic Editor: Amparo López Jiménez

Received: 17 May 2022 Accepted: 10 June 2022 Published: 11 June 2022

Publisher's Note: MDPI stays neutral with regard to jurisdictional claims in published maps and institutional affiliations



Copyright: © 2022 by the authors. Licensee MDPI, Basel, Switzerland. This article is an open access article distributed under the terms and conditions of the Creative Commons Attribution (CC BY) license (https://creativecommons.org/licenses/by/4.0/).

1. Introduction

One of the standard active flow/heat control techniques is by means of localized wallnormal perturbations in wall-bounded flows (Kral [1], Gad-el-Hak [2] and more recently Greenblatt et al. [3]). Furthermore, the impact of blowing on turbulent coherent structures is a crucial topic in active flow control since large-scale motions (LSM) usually carry most of the turbulent kinetic/thermal energy of the flow (Balakumar and Adrian [4] and Hutchins and Marusic [5]). As a consequence, by controlling these coherent motions, significant modifications to the velocity and thermal fields can be achieved, with possibly minimal energy input. According to Corke and Thomas [6], several studies to reduce skin-friction drag in wall-bounded turbulent flows by using surface blowing/suction have tried to manipulate the ejection and sweep events, considered the heart of the Reynolds stress production [7,8]. A typical case of active flow control by local three-dimensional blowing perturbations is the jet in turbulent crossflow. A complex set of turbulent motions and vortical structures is developed by the interaction of the jet with the crossflow (Fric and Roshko [9]): the shear-layer vortices, the counter-rotating vortex pair (CVP), the wake vortices and the horseshoe vortex, and are sketched in Figure 1. These vortex structures have been the motivation of several studies by many researchers: Fric and Roshko [9], Kelso et al. [10], Karagozian [11], New et al. [12], Muldoon and Acharya [13] and Sau and Mahesh [14]. For instance, vortex-generator jets (VGJs) are employed in low-pressure turbines to mitigate flow separation in diffusers by injecting "streamwise momentum" in turbulent boundary layers subject to an adverse pressure gradient [15]. A skew-angle

Energies **2022**, 15, 4296 2 of 30

VGJ creates a counter-rotating vortex pair with one dominant strong leg, while the other is of opposite sign and weak. This strong streamwise coherent structure can be used to redistribute high-momentum freestream fluid down to the near-wall region in order to energize the separating boundary layer [15].

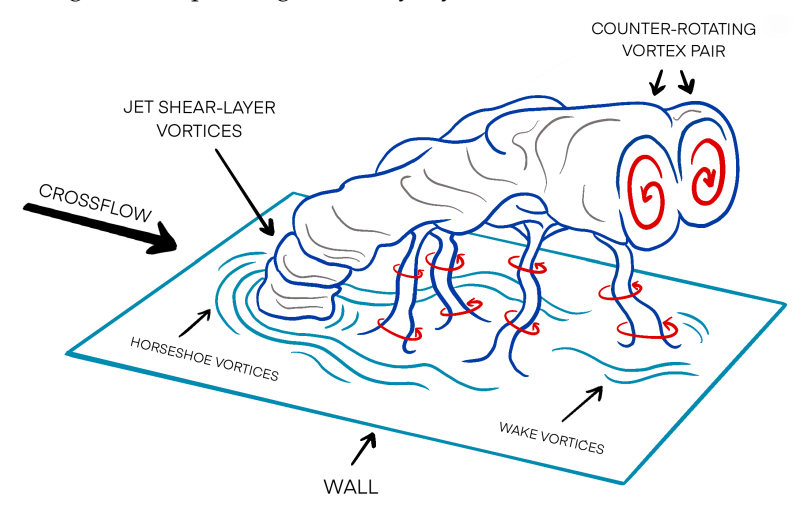


Figure 1. Schematic of the different types of vortical structures in a crossflow jet. Adapted from [9].

Furthermore, film cooling is a classical example of a crossflow jet applied to turbomachinery and rocket propulsion (Wernet et al. [16] and Ye et al. [17]). The idea is to inject cool air by means of small surface holes in such a way as to create a protecting layer between the surface and the hot combustion gases. Whereas high velocity or blowing ratios are set in vortex-generator jets, in the film cooling technique, low blowing ratios are generally prescribed to maintain the jet wake or protecting layer very close to the surface. Comprehensive summaries on film cooling studies can be found in review articles by Goldstein [18] and Bunker [19]. The injected air typically possesses a different velocity and temperature than those of the freestream flow, yielding a flow field with high turbulence and large temperature differences (Shyam et al. [20]). These turbulent fluctuations have been shown experimentally to affect the downstream properties of the crossflow fluid (Kamotani and Greber [21]).

The most important vortical structure that emerges in the crossflow-jet interaction is definitely the CVP. In fact, there is a detrimental effect of the CVP on the effectiveness of the downstream wall since vertical mixing is enhanced. Therefore, significant research effort has been invested in order to assess the effects of different external conditions on CVP. For instance, Johnson and Shyam [22] performed LES and RANS (SST turbulence model) of film cooling at different blowing ratios. They found better predictions by the LES approach, particularly for the spanwise and normal spreading of the jet in the nearhole region. Smith and Mungal [23] experimentally studied the trajectory, scaling and structure of crossflow jets at very high-velocity ratios from extensive imaging of the planar concentration field. Bagheri et al. [24] carried out an analysis on the three-dimensional formation and stability of vortices formed during the interactions of jets in crossflow. They concluded by means of selective frequency damping that high-frequency unstable global eigenmodes were associated with shear-layer instabilities on the CVP; meanwhile, low-frequency modes were linked to shedding vortices in the wake of the jet. According to Mahesh [25], the flow structure at low-velocity ratios might be essentially different from the generally accepted vortex system mentioned above. Recent advances in flow simulations with high spatial-temporal resolution (i.e., direct numerical simulations or DNS) have opened up the possibility of enhancing the insights behind jets in crossflow (Muppidi and Mahesh [13,26], Liu et al. [27]). Certainly, one of the major influences on the downstream development of jet wakes is the presence of a streamwise pressure gradient. Coletti et al. [28] conducted experiments on an inclined turbulent jet discharging a passive scalar into a turbulent crossflow subject to favorable (FPG), zero (ZPG) and adverse

Energies **2022**, 15, 4296 3 of 30

(APG) streamwise pressure gradients. They concluded that under FPG, the jet trajectory significantly bent toward the wall. While the latter enhances the film cooling performance, the CVP fortification and boundary layer shrinking due to flow acceleration caused vertical mixing augmentation, a negative aspect of the film cooling technique.

In summary, the crucial role of external conditions, such as streamwise pressure gradients, on the jet in turbulent crossflow has been established; however, the literature regarding this issue is rather scarce, particularly in passive scalar transport due to crossflow jets. Furthermore, Direct Numerical Simulation (DNS) represents an important numerical tool to obtain exhaustive information on turbulent boundary layers, particularly in the near-wall region where the majority of the experimental techniques possess spatial resolution limitations. Therefore, the main purpose of the present study is to understand the physics behind localized 3D blowing perturbations under the presence of very strong FPG at two different velocity ratios (VR = 0.5 and 1). The extensive data supplied by DNS allow us to elucidate the effects of strong flow acceleration on the complex vortex system generated downstream of a crossflow jet and to gain better knowledge of the turbulence intensities, Reynolds shear stresses, temperature variance and momentum/thermal coherent structures.

2. Mesh Generation, Flow Solver, Inflow Generation and Boundary Conditions

Capturing the physics of turbulent spatially-developing boundary layers by using DNS is not a trivial task due to the following reasons: (i) high mesh resolution is required in order to resolve the smallest turbulence scales (Kolmogorov and Obukhoff–Corrsin scales), (ii) the computational box must be large enough to appropriately resolve the influence of the turbulent "superstructures" (Hutchins and Marusic [29]) located in the outer region of the boundary layer, (iii) realistic time-dependent inflow turbulent conditions must be prescribed. Figure 2 shows a schematic of the computational domain in order to simulate the crossflow–jet interaction under a strong, favorable pressure gradient (FPG), which is prescribed by a top converging surface (sink flow). Without the prescription of any flow perturbation as in Araya et al. [30] (i.e., vertical jet), the infringed flow acceleration in this region is so strong that turbulent intensities are significantly attenuated; however, the turbulence residual remains non-negligible with a logarithmic behavior of the Reynolds shear stresses. It was found in [30] that the flow state was "laminarescence", an earlier stage of the quasi-laminarization process, according to Narasimha and Sreenivasan [31].

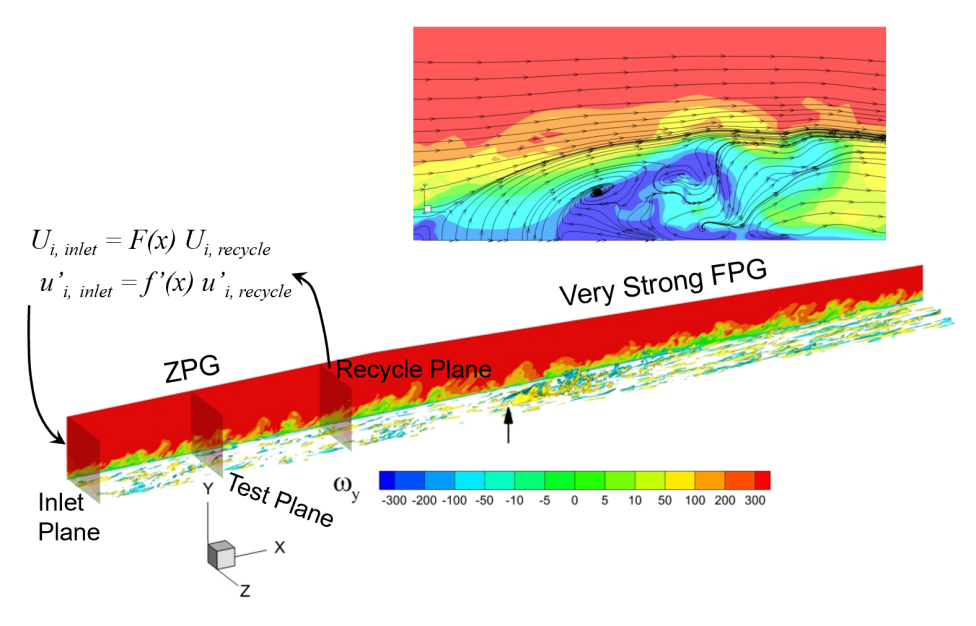


Figure 2. Schematic of the spatially-developing boundary layer with inlet, recycle and test planes about $60\delta_{inl}$ in streamwise length. The top view shows a close-up of the crossflow jet.

Energies **2022**, 15, 4296 4 of 30

The strong formulation of the dimensionless instantaneous governing equations utilized in the present investigation for incompressible flows is as follows,

$$\frac{\partial U_i}{\partial x_i} = 0, \tag{1}$$

$$\frac{\partial U_i}{\partial t} + U_j \frac{\partial U_i}{\partial x_j} = -\frac{\partial P}{\partial x_j} + \frac{1}{Re_\theta} \frac{\partial^2 U_i}{\partial x_j^2},\tag{2}$$

$$\frac{\partial \Theta}{\partial t} + U_j \frac{\partial \Theta}{\partial x_j} = \frac{1}{PrRe_{\theta}} \frac{\partial^2 \Theta}{\partial x_j^2}, \tag{3}$$

where the Einstein summation convention is applied. U_i is the dimensionless velocity component in the x_i direction, $\Theta = (T - T_w)/(T_\infty - T_w)$ is the dimensionless temperature difference, P is the dimensionless pressure, t is the dimensionless time and x_i is the dimensionless spatial coordinate in the i direction, respectively. $Re_\theta = U_\infty \theta/\nu$ is the Reynolds number based on the freestream velocity, U_∞ , and the inlet momentum thickness θ . Pr is the molecular Prandtl number. In the governing equations, the parameters are normalized based on the freestream velocity, U_∞ , the freestream temperature, T_∞ , the wall temperature, T_w and the inlet momentum thickness, θ_{inlet} .

Flow Solver: To successfully perform the proposed DNS, a highly accurate, very efficient, and highly scalable CFD solver is required. PHASTA (Parallel Hierarchic Adaptive Stabilized Transient Analysis) is an open-source, parallel, hierarchic (2nd to 5th-order accurate), adaptive, stabilized (finite-element) transient analysis tool for the solution of compressible [32] or incompressible flows (Jansen [33]). The flow solver PHASTA has been defined by considering a stabilized finite element method in space to spatially discretize the incompressible Navier–Stokes equations with a Streamline Upwind Petrov–Galerkin (SUPG) stabilization. Furthermore, the weak formulation of the problem creates a system of nonlinear ordinary differential equations, which are discretized in time via a generalized- α time integrator generating a nonlinear system of algebraic equations. Additionally, this system is linearized by Newton's method, which yields a linear algebraic system of equations, as follows:

$$\begin{bmatrix} K & G \\ -G^T & C \end{bmatrix} \begin{bmatrix} \Delta \dot{u} \\ \Delta \dot{p} \end{bmatrix} = - \begin{bmatrix} R_m \\ R_c \end{bmatrix}, \tag{4}$$

where matrix K derives from the tangent of the momentum equation with respect to the acceleration, G derives from the tangent of the momentum equation with respect to the pressure time derivative, and G derives from the tangent of the continuity equation with respect to pressure time derivative. The matrices G0 and G0 are the momentum and continuity residuals, respectively. Equation (4) can be solved monolithically; however, the required tight tolerance makes this approach almost impractical. Consequently, a more feasible alternative consists in approximately solving a preconditioned system. Thus, the equation for G1 is obtained by static condensation of Equation (4), leading us to the discrete pressure Poisson equation (PPE):

$$\left[G^T\hat{K}^{-1}G + C\right]\Delta\dot{p} = \left[-G^T\hat{K}^{-1}R_m - R_c\right],\tag{5}$$

where \hat{K}^{-1} is an approximation of K^{-1} obtained by considering only the diagonal entries of K^{-1} . The linear equation system (5) is first solved by the Conjugate Gradient (CG) method. Later, the system of Equation (4) is computed by the GMRES method. Moreover, the fully coupled momentum and continuity equations are solved with multiple nonlinear iterations (two nonlinear iterations are performed on each step) and an additional discrete pressure Poisson equation between each iteration to maintain a tight tolerance on the continuity equation ([34,35]). Once the velocity/pressure field is converged at each timestep, the passive scalar field is solved via three linear iterations. Although higher orders of accuracy could be achieved with PHASTA by selecting appropriate elements, in practice,

Energies **2022**, 15, 4296 5 of 30

linear elements were used, which yielded global second-order accuracy in space. In all cases, the meshes are structured with hexahedral elements, which show excellent performance in turbulent flow simulations. The code is second-order accurate in time.

The flow solver has been extensively validated in a suite of DNS of turbulent boundary layers with high spatial/temporal resolution [30,36–39]. The reader is referred to [40] for more details about the numerical aspects of the finite element approach followed by PHASTA.

Inflow Generation: One of the vital features of the simulations of unsteady spatiallydeveloping boundary layers (SDTBL) is the prescription of accurate and realistic turbulent inflow information. In this study, we are employing the inflow generation method devised by Araya et al. [36], which is an improvement to the original rescaling-recycling method by Lund et al. [41]. The seminal idea of the rescaling–recycling method is to extract the flow solution (mean and fluctuating components of the velocity and thermal fields) from a downstream plane (called "recycle"), and after performing a transformation by means of scaling functions, the transformed profiles are re-injected at the inlet plane. The rescaling process requires prior knowledge about how the velocity/temperature and length scales are related between the inlet and recycle stations. We proposed a dynamic approach in which such information is deduced dynamically by involving an additional plane, the so-called test plane located between the inlet and recycle stations, as seen in Figure 2. In the composite computational domain shown, a ZPG zone (the turbulence "precursor") is attached well upstream of the location of the wall-normal jet. This strategy of prescribing an equilibrium ZPG zone allows realistic turbulent conditions to be fed into the non-equilibrium region with a transverse jet.

Boundary Conditions: At the wall, the classical no-slip condition is imposed for velocities. An isothermal condition is prescribed for the temperature field at the wall, which is assumed a passive scalar. The lateral boundary conditions are handled via periodicity. The pressure is weakly prescribed at the outlet plane. At the top inclined surface (shear-less), the normal component of the velocity is prescribed a zero value (streamline) and freestream value for temperature. For the ZPG zone, freestream values are assumed for the streamwise velocity and temperature while zero-vertical gradient for the remaining velocity components. As conducted by Bagheri et al. [24], here, the jet is modeled by imposing a wall-normal velocity at the surface in a circle with a radius R. In the present investigation, the radius is approximately half of the inlet boundary layer thickness, i.e., $R \approx \delta_{int}/2$. The velocity ratio (VR) is defined as the ratio between V_{max} and the incoming freestream velocity, U_{∞} . We are considering two different velocity ratios, i.e., VR = 0.5 and 1. The Reynolds numbers Re_D based on the pipe diameter (2R) and V_{max} are 1520 and 3040 at VR = 0.5 and 1, respectively. At the lower velocity ratio, since the Re_D is lower than the critical value for pipe flows, a parabolic velocity profile, V(r), is prescribed for the laminar jet as follows;

$$V(r) = V_{max}[1 - (r/R)^2] (6)$$

where r is the distance to the jet center, and V_{max} is the surface velocity at the jet center. For the unitary velocity ratio, a turbulent jet is set, based on the DNS study by Wu and Moin [42], at $Re_D = 5300$. Figure 3 shows the distribution of the prescribed vertical velocity at the jet location for both velocity ratios, with a flatter and more homogeneous velocity distribution for the turbulent jet or VR = 1. Furthermore, the dimensionless temperature of the jet (coolant) is prescribed as $\Theta_{coolant} = -0.5$, while the normalized wall temperature is $\Theta_w = 0$ and the normalized freestream temperature is $\Theta_\infty = 1$.

Energies **2022**, 15, 4296 6 of 30

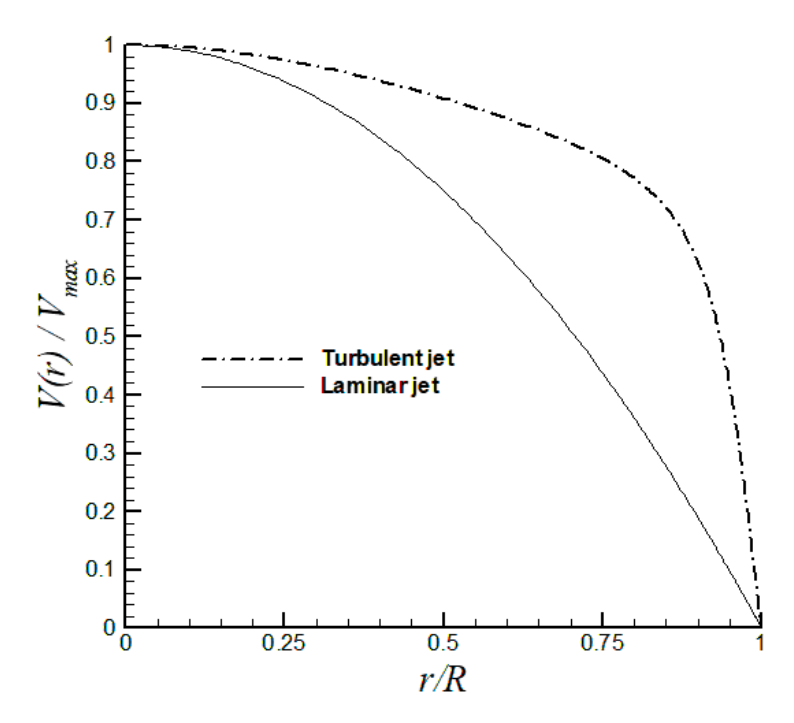


Figure 3. Wall-normal velocity distribution prescribed at the jet location.

Table 1 summarizes the characteristics of the analyzed three (3) cases. One Baseline case is run (Case 1) by prescribing a zero pressure gradient (ZPG) on the transverse jet region, which means a constant cross-sectional area of the computational domain. The purpose of the Baseline case is to evaluate the effects of the streamwise pressure gradient on the downstream development of the jet wake. Information regarding the computational domain dimensions in terms of the inlet boundary layer thickness δ_{inl} (where L_x , L_y and L_z represent the streamwise, wall-normal and spanwise domain length, respectively) and the mesh resolution in wall units (Δx^+ , Δy_{min}^+ , Δz^+) is also supplied based on the inlet friction velocity. Readers are referred to Appendix A for suitability of the mesh resolution and time step as well as numerical validation. Figure 4 depicts a typical mesh with a grid point distribution of $600 \times 80 \times 80$ for Case 2 and 3, while the point distribution was $440 \times 60 \times 80$ in Case 1. Note that the streamwise domain length (L_x) includes the ZPG precursor zone for inflow turbulent information generation, as previously mentioned, which demands approximately $20\delta_{inl}$ in all cases. Furthermore, the momentum thickness Reynolds number is approximately 400, just upstream of the transverse jet. The domain length was prescribed long enough (about $40-60\delta_{inl}$) in order to appropriately capture the influence of large-scale motions (LSM) [29]. By comparing Cases 2 and 3, the effect of the blowing strength is evaluated in FPG flows.

Table 1. Numerical cases.

Case	Type	VR	$L_x \times L_y \times L_z$	Δx^+ , Δy_{min}^+ , Δz^+
1	ZPG	0.5	$43\delta_{inl} \times 3.2\delta_{inl} \times 4.3\delta_{inl}$	14.3, 0.2, 7.95
2	FPG	0.5	$60\delta_{inl} \times 4.3\delta_{inl} \times 4.3\delta_{inl}$	14.27, 0.2, 7.9
3	FPG	1	$60\delta_{inl} \times 4.3\delta_{inl} \times 4.3\delta_{inl}$	15, 0.2, 8

Energies **2022**, 15, 4296 7 of 30



Figure 4. Schematic of the mesh in FPG cases.

3. Discussion of Results

The crossflow jet simulations were initiated from a previous unperturbed DNS case [30]. After approximately twelve flowthroughs, samples were collected during the last 1900 nondimensional time t^+ for statistics computation, totaling 1200 flow fields. A flowthrough is the time it takes for a freestream fluid parcel to go from the domain inlet to the outlet plane. Figure 5 shows the streamwise development of some indicators of the onset of relaminarization for Cases 2 and 3 without the transverse jet and focusing on the zone x/D > -7. The acceleration parameter $K\left(=\frac{v}{U_{\infty}^2}\frac{dU_{\infty}}{dx}\right)$ rises abruptly at the ZPF–FPG intersection (18 $\leq x/\delta_{inl} \leq$ 26) to finally asymptote to the constant value of 4.0×10^{-6} , beginning at $x/\delta_{inl} \approx 30$. Based on [43], the present flow should have been relaminarized (since $K > 3.0 \times 10^{-6}$); however, the C_f never achieves the laminar value for sink flows, as discussed in [30]. The critical K value of 3.5×10^{-6} suggested by Kline [44] was achieved around $x/\delta_{inl} \approx 25$. Furthermore, the critical value of -0.025 for $\Delta p = \frac{v dP/dx}{u_T^3}$ [45] was reached at $x/\delta_{inl} \approx 34$. Narasimha and Sreenivasan [31] introduced the parameter $\Lambda = \frac{-\delta dP/dx}{\tau_{wo}}$ (where δ and dP/dx are local values of the boundary layer thickness and the streamwise pressure gradient, respectively; τ_{wo} is the wall shear stress at the last ZPG station, upstream of the FPG region), defined as the ratio of the pressure gradient dP/dxto the characteristic Reynolds stress gradient τ_{wo}/δ . Thus, no prior knowledge of turbulent stresses was required to describe the mean flow. For large values of Λ (\geq 50), they demonstrated that the mean flow field could be split into an inner laminar sub-layer and an inviscid but rotational outer layer and used this criterion as an identifier of reversion. Nevertheless, the maximum computed value of Λ (\sim 22) is lower than the laminarization indicator of $\Lambda_c = 50$ proposed by [31]. Consequently, previous indicators of the relaminarization onset K, Δp and $\Delta \tau$ have predicted relaminarization in our FPG region, except for the Λ parameter by [31]. More specifically, our strong FPG flow might be located within the "laminarescent" region (b) of [31], just upstream of the relaminarization onset, which is consistent with the Λ -computed values lower than 50 [30].

Figure 6a,b depicts the time-averaged static pressure with respect to the outlet pressure (P/P_{outlet}) at different vertical locations (i.e., at $y^+ = 5$ and 50, respectively). The vertical dashed lines indicate the jet boundaries. Here, the streamwise coordinate x has been normalized by the jet diameter, D. Well upstream of the jet, it can be seen that the mean pressure remains constant, as a ZPG zone was imposed for turbulent inflow generation. These constant values in all three cases "accommodate" themselves to the "weakly" prescribed outflow pressure and strongly depend on the imposed velocity ratio (VR) at the jet. Clearly, the higher the velocity ratio, the larger the upstream pressure and pressure drop through the jet. As the incoming turbulent flow approaches the jet, the constant injection of fluid induces adverse pressure gradient (APG) zones upstream and downstream of the jets (flow deceleration). These are the spikes in pressure that are observed. In contrast, the flow is significantly accelerated over the jets due to the presence of favorable pressure gradient (FPG), thus producing a drop in pressure within the jet. For Case 1, it can be seen that the APG zone close upstream of the jet is situated around -2 < x/D < -0.5, with a maximum value in the order of $P/P_{outlet} \approx 1.15$, whereas the APG region close downstream of the jet is within 0.5 < x/D < 3 with an "overshoot" of $P/P_{outlet} \approx 1.05$ in relative pressure in the near-wall region (e.g., $y^+ = 5$ for Case 1). In the other two cases

Energies **2022**, 15, 4296 8 of 30

(i.e., Cases 2 and 3), the APG regions are seen as well before and after the jet with longer and more evident streamwise lengths and peak values. As one moves farther from the wall, i.e., at $y^+ = 50$ in the buffer region in Figure 6b, a similar picture of the pressure distribution is observed in all cases, with larger variations in peaks of pressure for Case 3. This is explained by the fact that a bigger velocity ratio (VR = 1) was imposed in Case 3 with respect to the other two Cases 1 and 2 (VR = 0.5). Therefore, the injected fluid can penetrate further into the incoming turbulent boundary layer, causing important changes in the buffer and log regions. However, the streamwise zone of influence of APG is very short downstream of the jet, around 3D in length. Focusing on the well downstream zone from the jets, mean pressure tends towards the outflow value and quickly recovers the prescribed streamwise pressure gradient. In Case 1, where a zero pressure gradient was also imposed downstream, this pressure recovery occurs within four to five D's from the jet. On the other hand, for Cases 2 and 3, a strong streamwise favorable pressure gradient (FPG) was prescribed downstream (with the acceleration parameter K equal to 4×10^{-6} , as described in Figure 5). The pressure recovery after the flow perturbations caused by the jet takes much longer ($\approx 15D$).

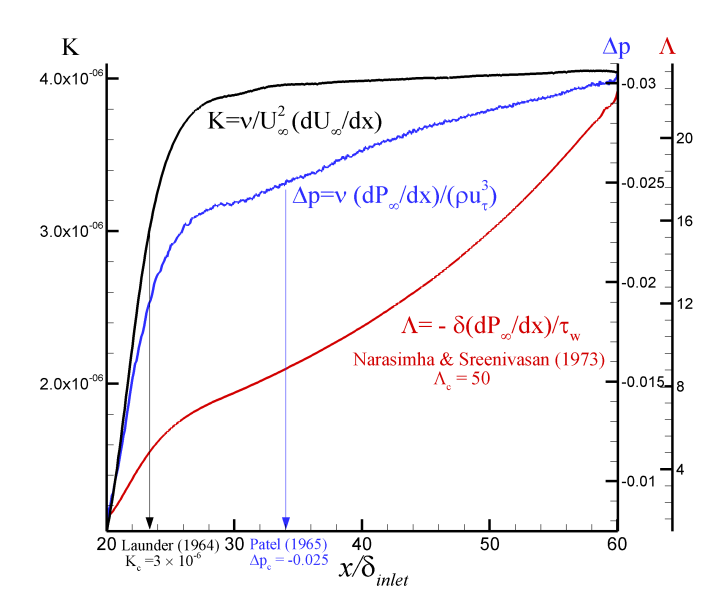


Figure 5. Streamwise variation of K, Δ_p , and Λ .

From Figure 7, it is seen that the freestream velocity (U_∞) is normalized by its inlet value in the three cases analyzed. All three cases have a constant behavior of $U_\infty/U_{\infty,inlet}$ up to 7D upstream of the jet. At this point, Cases 2 and 3 begin experiencing the effects of their FPG, thus being accelerated. The freestream velocity increases with a power law of the distance from the beginning of the imposed FPG or acceleration parameter K, reaching an 80% increase by the end of the computational domain, whereas the freestream velocity remains approximately constant in Case 1 under ZPG conditions. Case 1 exhibits an increase once it encounters the jet, but these effects are approximately depleted by 10D, and the relative free stream velocity returns back to the unitary value. For Cases 2 and 3, there are jumps in the freestream velocity within and after the jet, more noticeably in Case 3 due to the higher momentum flux injected. These jumps are due to the drop in pressure in this area, which is caused by the momentum injection of the jet. Case 3 exhibits an evident "upward bump" due to the larger momentum fluid injection. However, these perturbations do not last longer and by 10-15D downstream of the jet, the differences in $U_\infty/U_{\infty,inlet}$ between Cases 2 and 3 are completely negligible.

Energies **2022**, 15, 4296 9 of 30

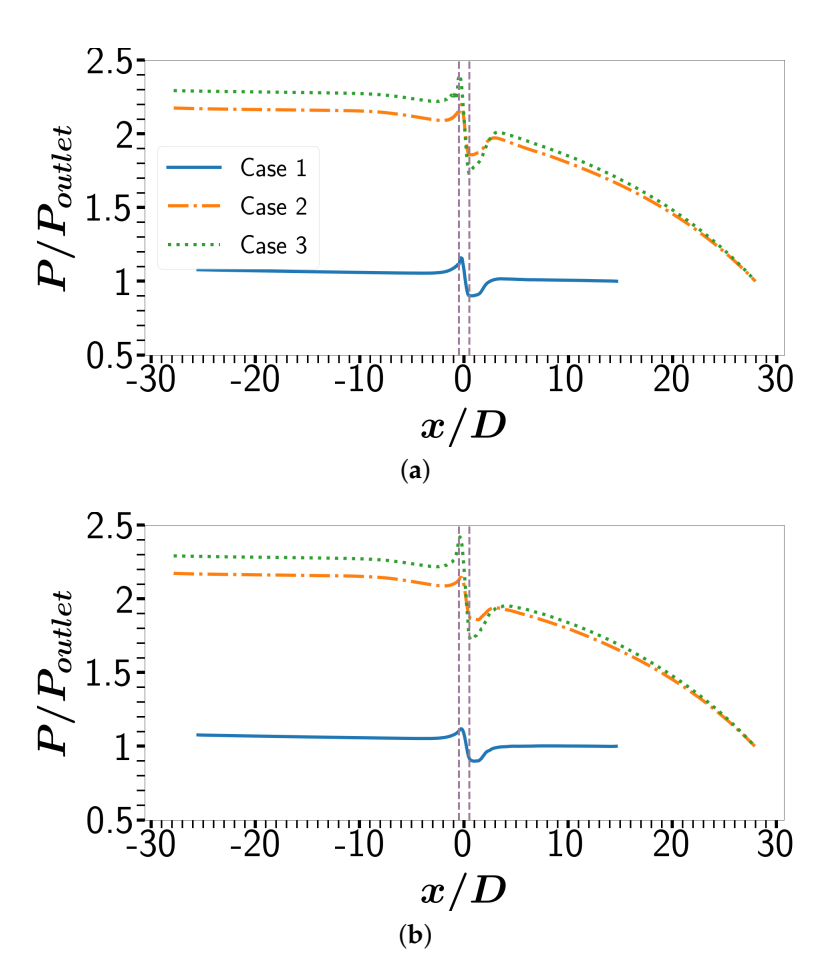


Figure 6. Mean pressure in all cases at (a) $y^+ = 5$ and (b) $y^+ = 50$.

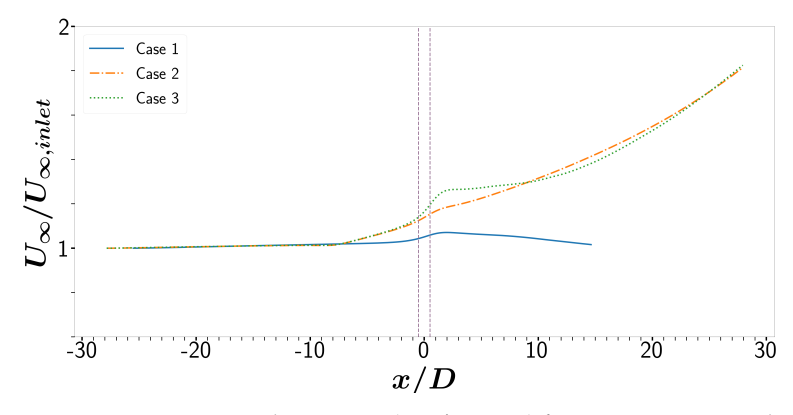


Figure 7. Freestream velocity ratio $(U_{\infty}/U_{\infty,inlet})$ for Case 1, Case 2 and Case 3.

The momentum thickness in incompressible flow is defined as,

$$\theta = \int_0^\infty \frac{U}{U_\infty} \left(1 - \frac{U}{U_\infty} \right) dy \tag{7}$$

where U is the mean streamwise velocity and U_{∞} is the freestream velocity. The momentum thickness, θ , represents the loss of the incoming flow momentum due to the presence of a solid wall and the no-slip condition in the fluid–wall interaction caused by the fluid viscosity. It represents a very important integral boundary layer parameter since it can be demonstrated that θ is proportional to the drag force infringed on the body. Further-

Energies **2022**, 15, 4296 10 of 30

more, based on the length scale θ , the following momentum-thickness Reynolds number is defined;

$$Re_{\theta} = \frac{\rho U_{\infty} \theta}{\mu} = \frac{U_{\infty} \theta}{\nu} \tag{8}$$

Figure 8 presents the momentum–thickness Reynolds number (Re_{θ}) for all three cases. Upstream of the vertical jet, Re_{θ} profiles exhibit the typical linear increase in the canonical boundary layer (ZPG). The presence of flow deceleration just before the jet induces APG and, consequently, a growth of the boundary layer and momentum thickness. The strong acceleration (FPG) infringed in the flow over the jet makes the boundary layer thinner, reducing Re_{θ} locally. An obvious recovery on Re_{θ} profiles can be observed in the near downstream region of the jet.

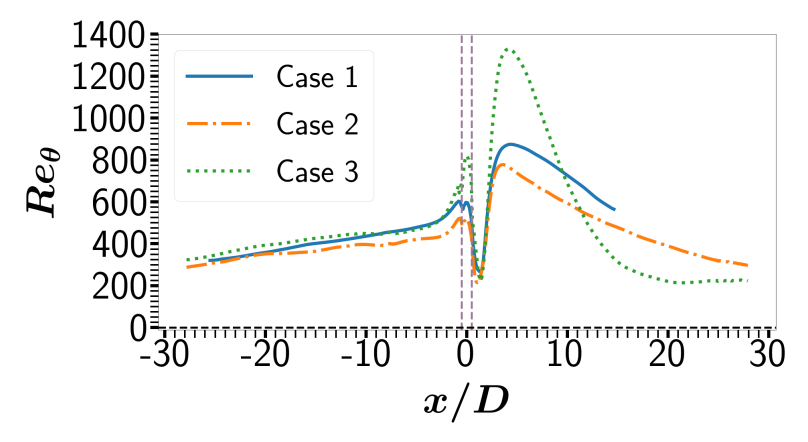


Figure 8. Streamwise variation of Re_{θ} for Case 1, Case 2 and Case 3.

The friction velocity u_{τ} is defined as follows,

$$u_{\tau} = \sqrt{\frac{\tau_w}{\rho}} \tag{9}$$

where ρ is the density of the fluid, and τ_w is the wall shear stress given by

$$\tau_w = \mu \frac{\partial U}{\partial y} \bigg|_{vall} \tag{10}$$

where μ is the fluid dynamic viscosity, U is the mean streamwise velocity,, and y is the vertical distance from the wall. Furthermore, the skin friction coefficient was calculated as follows:

$$C_f = \frac{\tau_w}{\frac{1}{2}\rho U_\infty^2} = 2\left(\frac{u_\tau}{U_\infty}\right)^2 \tag{11}$$

The streamwise variation of the skin friction coefficient, C_f , is shown in Figure 9 for all cases in the centerline (mid YX-plane). The C_f parameter is based on the mean streamwise velocity, which has only been averaged in time. It can be seen that the skin friction coefficient C_f remains approximately constant up to x/D = -3, as expected for smooth ZPG boundary layers. However, C_f sharply begins decreasing at x/D = -2 in all cases due to the strong flow deceleration in the near-wall region caused by the presence of the jet. The vertical dashed lines indicate the edge locations for the transverse jet. Steady blowing perturbations by the jet provoke zones of Adverse Pressure Gradient (APG) just upstream and downstream in the near-wall region (i.e., flow deceleration), whereas the flow is significantly accelerated over the jets, according to [27]. This is the reason for the sharp decreases in C_f upstream and downstream of the jet, while the skin friction coefficient abruptly increases over the jet (FPG). Notice the effect of the streamwise pressure gradient on the downstream development of C_f : the presence of the FPG provokes a slower recovery

Energies 2022, 15, 4296 11 of 30

or monotonic decay. In addition, a large recirculation zone just downstream of the jet with negative values of C_f can be seen. In all three cases, the streamwise length of this recirculation zone is about 2D. The Stanton number is defined as follows,

$$St = \frac{q_w''}{\rho c_p U_{\infty}(\Theta_{\infty} - \Theta_w)}$$
 (12)

where q_w'' is the wall heat flux defined as:

$$q_w'' = -\left(k\frac{\partial T}{\partial y}\right)_{yy} \tag{13}$$

where k is the thermal conductivity of the fluid and $\partial T/\partial y$ is the thermal gradient at the wall in the y-direction. Figure 10 depicts the streamwise variation of the Stanton number for all three cases. Positive values of S_t mean that the fluid is transferring heat to the surface, while negative values indicate the opposite process. The variation of the Stanton number, S_t , exhibits a similar trend as C_f , which may reveal that the Reynolds analogy is somehow fulfilled but not completely satisfied since there is not an increase in S_t across the jet hole as in the C_f profile. This is consistent with previous conclusions from the literature since a very strong streamwise pressure gradient is a source of dissimilarity between the momentum and thermal field [37].

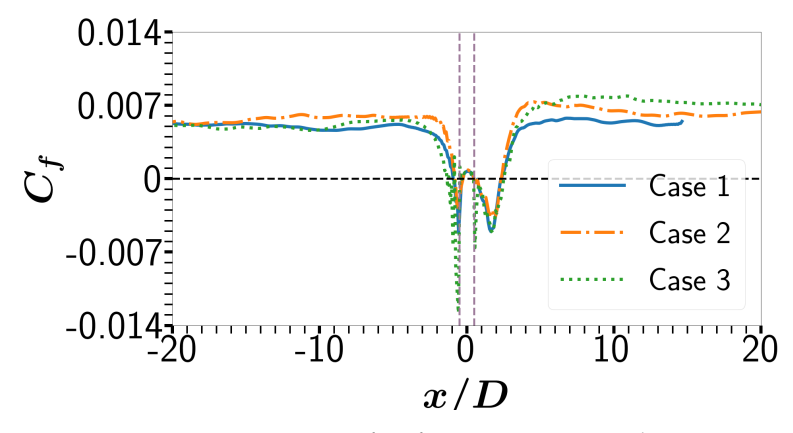


Figure 9. Streamwise variation of C_f for Case 1, Case 2 and Case 3.

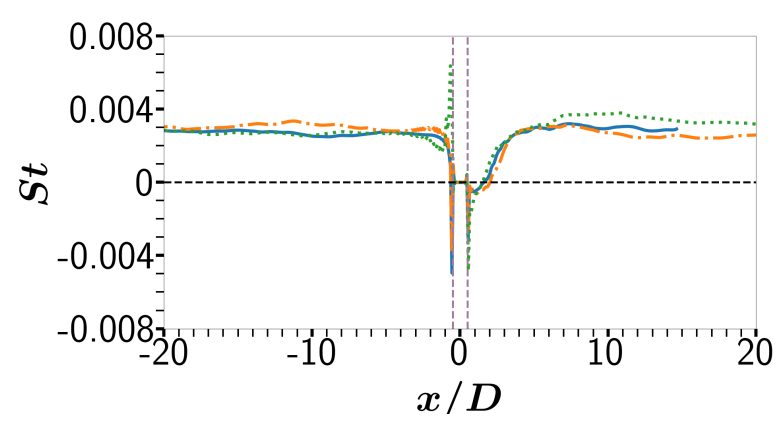


Figure 10. Streamwise variation of S_t for Case 1, Case 2 and Case 3.

Energies **2022**, 15, 4296 12 of 30

Figures 11–13 show how the streamwise velocity behaves from the wall to the freestream position and the dimensionless temperature difference (Θ) at varying streamwise distances from the jet center (x/D = -18, -1, 2 and 4). The mean streamwise velocity and temperature have been expressed in outer units, which means that freestream values are used in the normalization process. Furthermore, the vertical coordinate y is dimensionalized by the local boundary layer thickness δ . The corresponding flow profile at x/D = -18 can be considered the "baseline" profiles located far upstream of the jet (ZPG region). These baseline profiles are used to evaluate the distortion level exhibited after going through localized blowing perturbations. Readers should note the high level of similarity between U/U_{∞} and Θ profiles at x/D = -18, indicating that the Reynolds analogy is clearly satisfied. The physical reason is attributed to the no-presence of a streamwise pressure gradient and a nearly unitary value of the Prandtl number (Pr = 0.71). Moving closer to the vertical jet, for both U/U_{∞} and Θ profiles in Case 1, the values stay mostly positive at all distances. The only major differences are found at x/D = 2, where flow recirculation (flow separation in the mean flow is dictated by negative values of U) can be observed in the range $0.002 < y/\delta < 0.04$. At this location that is close to downstream of the jet, the injected momentum blocks the flow downstream, which causes flow retardation and separation. Case 2 presents almost the same behavior as Case 1, given that both have the same blowing ratio even though Case 2 is under FPG. The effect of flow acceleration in Case 2 can be described by a separation flow bubble "pushed" toward the wall. For Case 3, the situation significantly changes due to its high blowing ratio compared to the previous cases. The incoming boundary layer exhibited a strong deceleration, as seen in the negative U values of the profile at x/D = -1. At a distance of four diameters from the jet center, the streamwise velocity depicts significant distortion, with flow acceleration in the buffer layer and the presence of a "downward dip" around $y/\delta \approx 0.3$. This local flow deceleration is caused by the "encounter" of the jet trajectory with the freestream, inducing a shear layer. This means that when the outer inviscid and irrotational flow (coming from outside the turbulent boundary layer or TBL) penetrates into the TBL creating "valleys" (and "bulges"), it encounters the upward fluid motion by the streamwise vortices represented by the "legs" of the CVP, creating a stagnation point, and consequently, a shear layer. The reader is referred to Figure 2 (and its discussion) in the study by Lee et al. [46]. More discussion on this matter is supplied later on. In terms of the mean thermal profiles Θ , Case 1 exhibits a lengthy isothermal region between $0 < y/\delta < 0.4$ at x/D = 2. A zero value for the Θ parameter indicates that the local temperature corresponds to the wall temperature, according to the normalization considered. This is consistent with the local presence of flow recirculation or bubble, which curtails heat transfer. Note that the local Stanton number is zero. In Case 2, this isothermal region is significantly much smaller, ranging $0 < y/\delta < 0.2$ at x/D = 2. It is concluded that FPG makes the recirculation zone smaller along the vertical direction. On the other hand, Case 3 shows negative values of Θ around $y/\delta \approx 0.1 - 0.3$ at x/D = 2. It can be stated that the cold fluid emanating from the vertical jet $(\Theta = -0.5)$ has mixed with the incoming crossflow. In other words, these negative values in Θ mean that there is significant thermal mixing in these areas.

Figures 14–16 depict the root mean square (RMS) of flow fluctuations or turbulent intensities (i.e., u'^+_{rms} , v'^+_{rms} and Θ'^+_{rms}) as well as the Reynolds shear stresses ($-\langle u'v'\rangle^+$) for the three cases at x/D=-18, -1, 2 and 4. It is worth mentioning that flow statistics were computed in the centerline mid YX-plane and were only time-averaged (no spanwise averaging). Furthermore, local wall units were utilized. In general, rms of the streamwise and wall-normal components of the velocity fluctuations (u'^+_{rms} and v'^+_{rms}) are greatly enhanced just downstream of the jet, by a distance of two to four diameters. As expected, Case 3 with VR = 1 possesses the largest increases in u' and v'. It can be concluded that vertical transport of momentum is considerably intensified downstream of the jet. The almost six-fold increase in v'^+_{rms} peak values (as compared with the baseline profile at x/D=-18) for Case 3 supports the previous statement. Cases 1 and 2 possess the same velocity ratios (VR = 0.5) and exhibit similar degrees of increases in v'^+_{rms} and v'^+_{rms} . One may speculate

Energies 2022, 15, 4296 13 of 30

that there is not a concrete influence of streamwise pressure gradient on the velocity fluctuations in the near downstream region of the jet. However, previous conclusions may be scaling-dependent since the friction velocity (not shown) and skin friction coefficient are strongly attenuated by the recirculating flow. Interestingly, the $u_{rms}^{\prime+}$ and $\langle u'v' \rangle^+$ profiles at x/D = 2 and 4 in all cases show evident secondary outer peaks around $y^+ \approx 100$ –200, which is associated with the presence of a shear layer. According to Pope [47], turbulence events inside the boundary layer can be classified by quadrants as: Q1 or outward interactions (u' > 0 and v' > 0), Q2 or ejections (u' < 0 and v' > 0), Q3 or inward interactions (u' < 0and v' < 0), and Q4 or sweeps (u' > 0 and v' < 0). Here, u' is the instantaneous streamwise velocity fluctuation, whereas v' is the instantaneous wall-normal velocity fluctuation. The upward entrainment (Q2 motions) provoked by both streamwise vortices of the CVP and the inward Q4 motions induces a local flow deceleration and the formation of this shear layer. The presence of this shear layer significantly enhances turbulent mixing (Reynolds shear stresses) and thermal fluctuations. Clearly, the turbulence production is greatly augmented as well, since the major contributing component, i.e., the product of the Reynolds shear stress and the local velocity gradient $(\langle u'v' \rangle^+ \partial U^+ / \partial y^+)$, is boosted. The Reynolds shear stresses at x/D = 2 and 4 in Case 3 depict noticeable positive values (events in the Q1 and Q3 quadrants mostly contribute to the Reynolds shear stresses). Furthermore, the fact that u' and v' are positively correlated in the buffer-log region (20 < y^+ < 150) for Case 3 is attributed to the strong backflow. Case 2 has not shown the presence of positive $\langle u'v' \rangle^+$, while in Case 1, some positive values of $\langle u'v' \rangle^+$ were detected at x/D=2 and $y^+\approx 20$. It can be concluded that FPG counteracts the recirculation or backflow effect on developing positive cross-correlations on u' and v'.

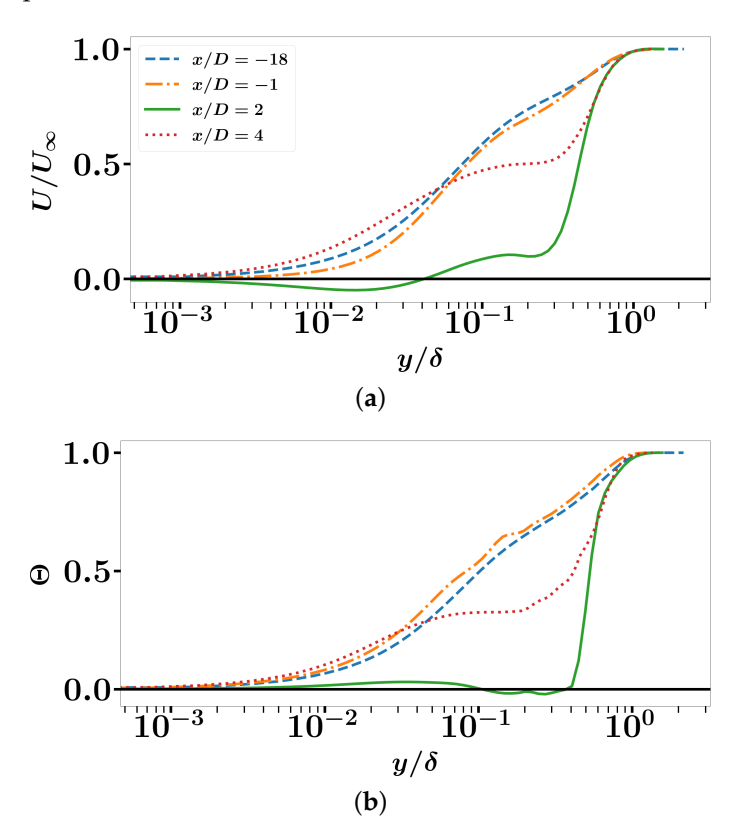


Figure 11. CASE 1: (a) mean streamwise velocity in wall units and (b) normalized mean temperature.

Energies **2022**, 15, 4296

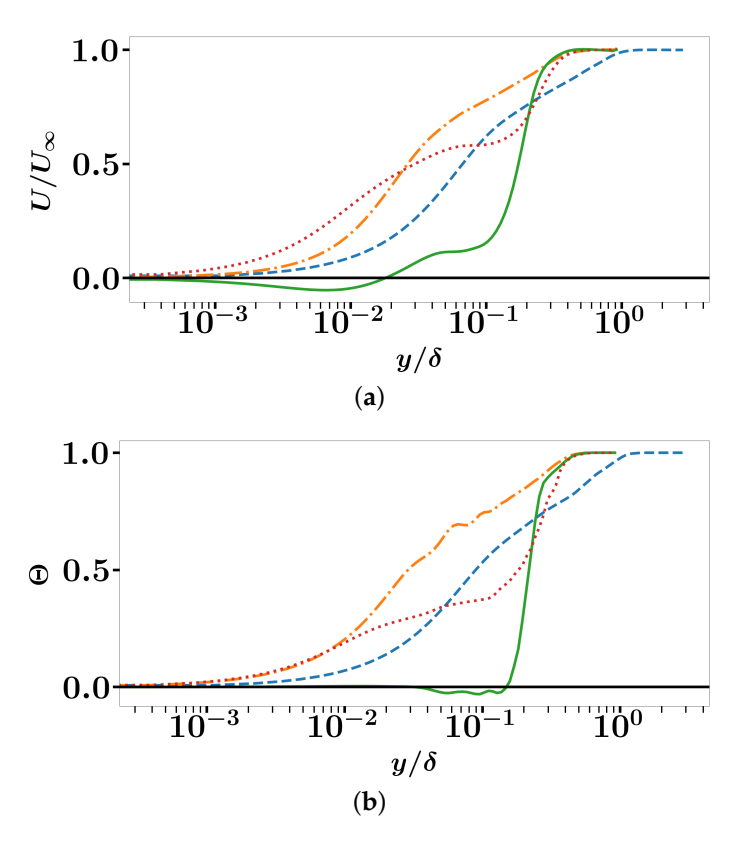


Figure 12. CASE 2: (a) mean streamwise velocity in wall units and (b) normalized mean temperature (profiles as in the legend of Figure 11a).

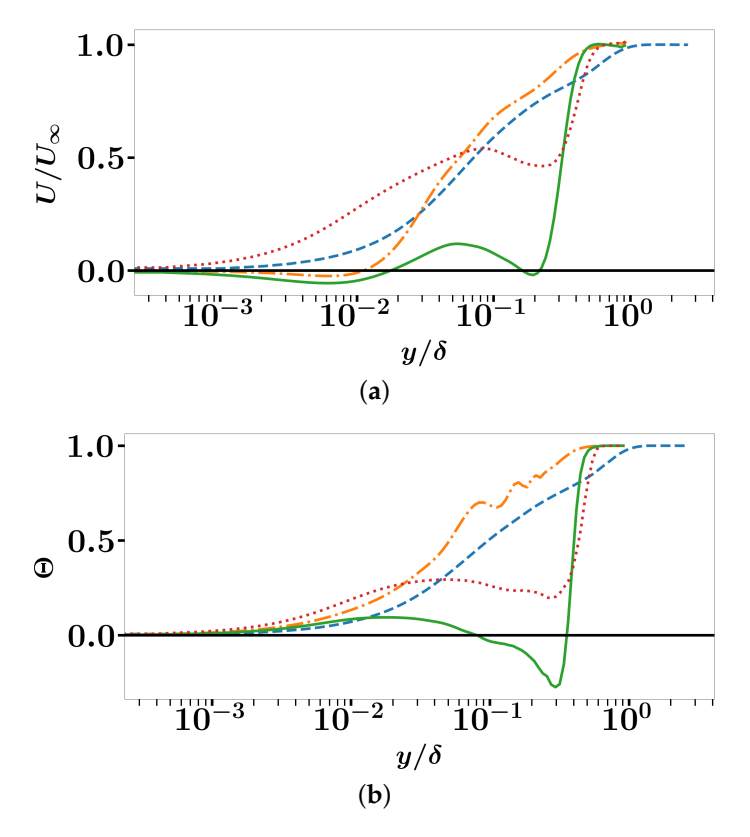


Figure 13. CASE 3: (a) mean streamwise velocity in wall units and (b) normalized mean temperature (profiles as in the legend of Figure 11a).

Energies **2022**, 15, 4296 15 of 30

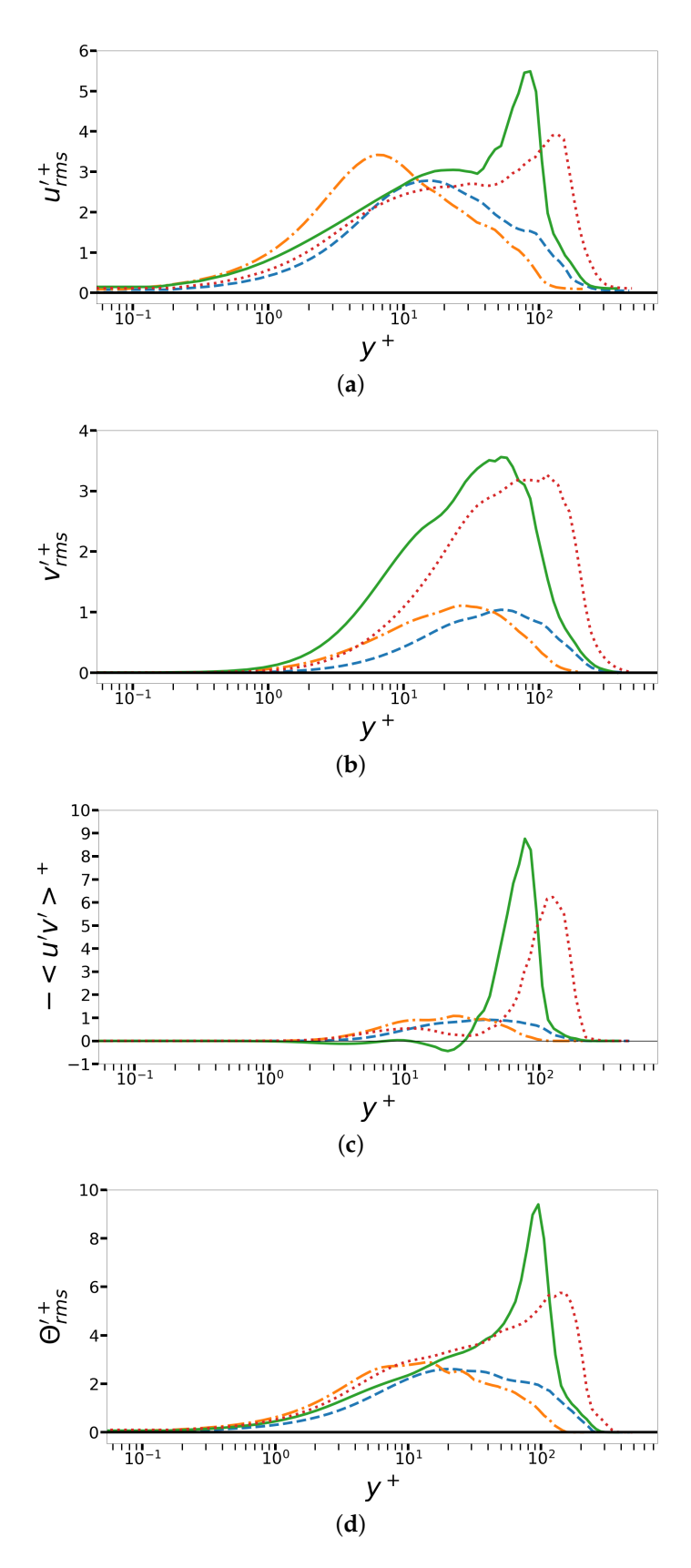


Figure 14. CASE 1: (a) RMS of streamwise velocity fluctuations, (b) RMS of wall-normal velocity fluctuations, (c) shear Reynolds stresses, and (d) RMS of thermal fluctuations (profiles as in the legend of Figure 11a).

Energies **2022**, 15, 4296

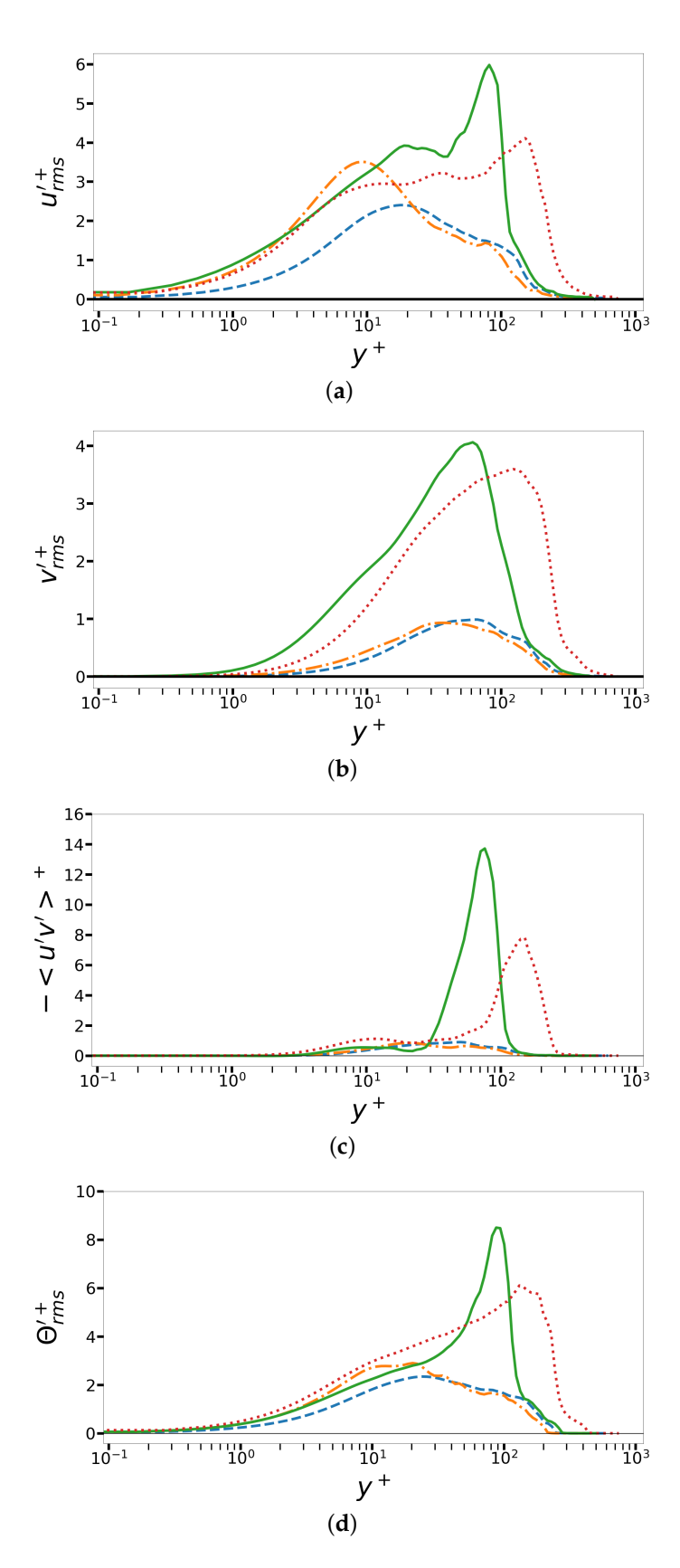


Figure 15. CASE 2: (a) RMS of streamwise velocity fluctuations, (b) RMS of wall-normal velocity fluctuations, (c) shear Reynolds stresses, and (d) RMS of thermal fluctuations (profiles as in the legend of Figure 11a).

Energies **2022**, 15, 4296 17 of 30

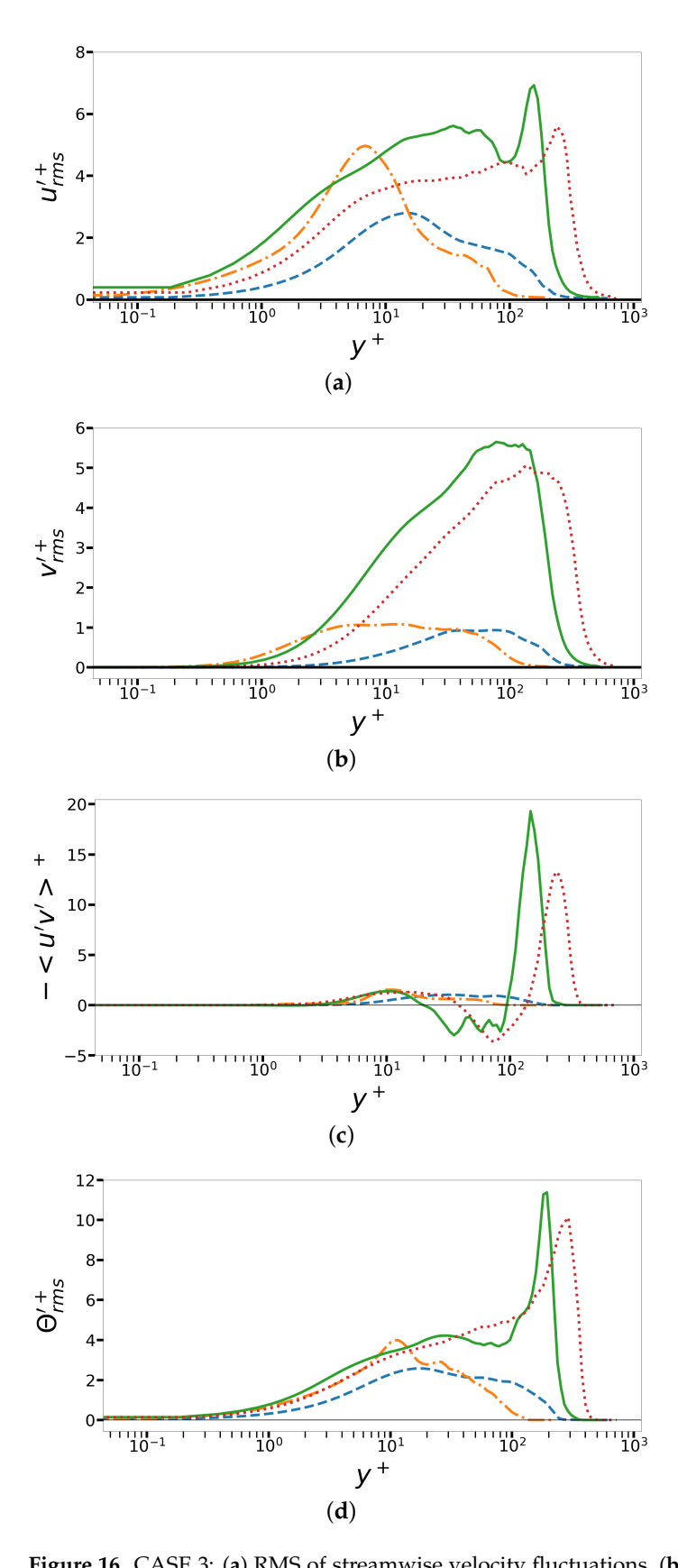


Figure 16. CASE 3: (a) RMS of streamwise velocity fluctuations, (b) RMS of wall-normal velocity fluctuations, (c) shear Reynolds stresses, and (d) RMS of thermal fluctuations (profiles as in the legend of Figure 11a).

Energies **2022**, 15, 4296 18 of 30

4. Turbulent Structure Visualization

A review article on organized motions in different types of turbulent flows was performed by Cantwell [48]. Flow visualization gives important insights into the turbulent structures in boundary layers. Moreover, it is well-known the key role of coherent structures as momentum and energy carriers. One of the most popular techniques for coherent structure identification was proposed by Hunt et al. [49], called the Q-criterion method. This criterion uses the velocity gradient (∇v) decomposition of:

$$\nabla v = S + \Omega \tag{14}$$

where S is the the rate-of-strain tensor ($S = \frac{1}{2}[\nabla v + (\nabla v)^t]$) and Ω is the vorticity tensor ($\Omega = \frac{1}{2}[\nabla v - (\nabla v)^t]$). They define a vortex as a spatial region where the Euclidean norm of the vorticity tensor, Ω , dominates that of the rate of strain, S. In other words, a vortex core is defined as the region with more flow rotation than strain. The Q-criterion can be summed up in the following equation:

$$Q = \frac{1}{2}(|\Omega|^2 - |S|^2) > 0 \tag{15}$$

Visualization of coherent structures by means of Q iso-surfaces colored by temperature is presented in Figure 17a-c for Case 1 (ZPG VR = 0.5), Case 2 (FPG VR = 0.5) and Case 3 (FPG VR = 1). Horseshoe vortices can be seen just upstream of the transverse jet. These structures are more elongated in Case 3 due to the strong flow acceleration (i.e., FPG). The interaction of the vertical transverse jet with the incoming turbulent boundary layer induces the generation of a complex vortex system or hairpin vortex packets downstream. For Case 3, with the higher flow perturbations, it can be seen that hairpin vortices are mostly responsible for transporting cold fluid injected by the jet (blue color). However, turbulence structures are weakened and nearly attenuated due to the strong flow acceleration provoked by the presence of FPG in Cases 2 and 3. The stabilizing effect provoked by the favorable pressure gradient is attributed to the dominance of the pressure gradient term over the turbulent transport term due to the shear Reynolds stresses in the x-momentum balance equation [30]. Furthermore, these coherent structures experience an evident stretching process along the streamwise direction and are forced to remain in the nea-wall and buffer layer since the time-averaged component of the wall-normal velocity *V* is significantly enhanced and points towards the wall. The most relevant observations can be summarized as follows:

- Turbulent structures are more elongated in Case 3 due to the strong flow acceleration (i.e., FPG). Furthermore, turbulent structures are weakened and nearly attenuated by FPG.
- 2. The interaction of the vertical transverse jet with the incoming turbulent boundary layer induces the generation of a complex vortex system or hairpin vortex packets downstream.

For the three cases that were studied, we wanted to evaluate how the injected momentum was vertically transported and convected downstream. Figure 18 shows contours of velocity magnitude at two distances from the jet center: x/D = 2 and 7.5. Furthermore, in the plane YZ, velocity vector plots are included. In all cases, and very close to downstream of the jet (i.e., at x/D = 2), the core of the counter-rotating vortex pair (CVP) is clearly observed. Notice the "mushroom"-like structure in Case 3 (deep blue zone). The CVP pumps up low-speed fluid, which encounters a downward motion, giving birth to a shear layer ($\sim Y/D = 1$) with low values of the fluid velocity. It has been previously explained that this shear layer enhances turbulence mixing and production. From the figures, it can be seen that at both velocity ratios VR = 0.5 and 1, the CVP structure went through a severe attenuation. It is interesting to see the strong downward motion (velocity vectors pointing

Energies **2022**, 15, 4296 19 of 30

towards the wall) in Cases 2 and 3, even in the outer part of the boundary layer (inviscid and irrotational region). This is caused by the prescription of strong FPG in sink flows.

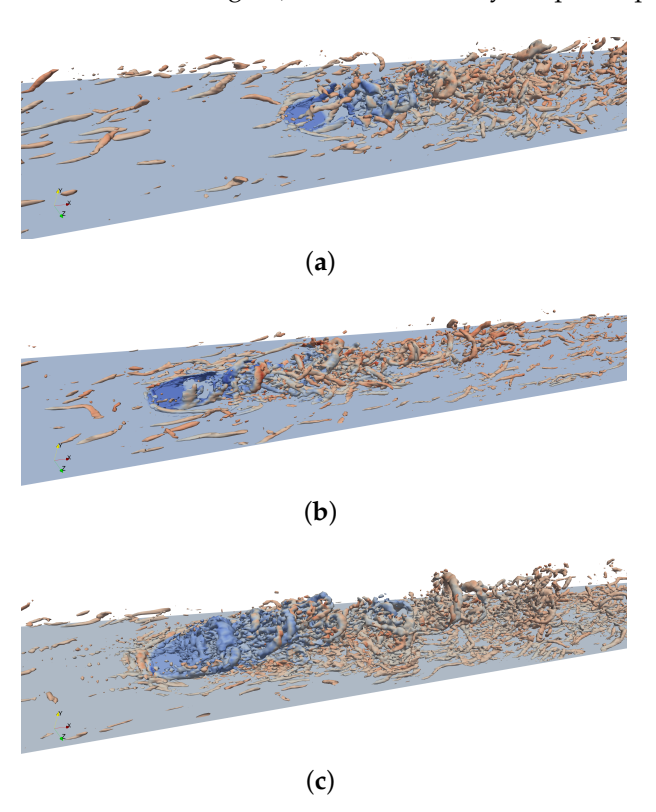
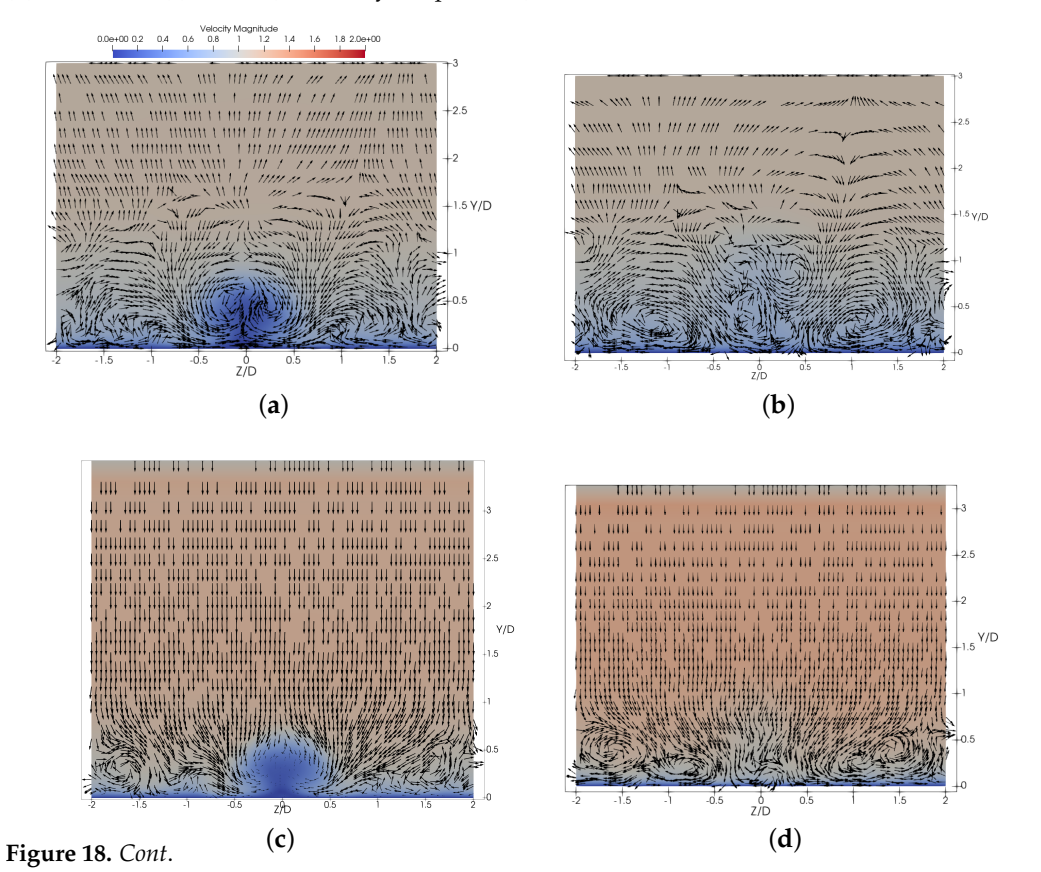


Figure 17. Visualization of coherent structures by means of *Q*—criterion iso-surfaces: (a) Case 1, (b) Case 2 and (c) Case 3 (colored by temperature).



Energies **2022**, 15, 4296 20 of 30

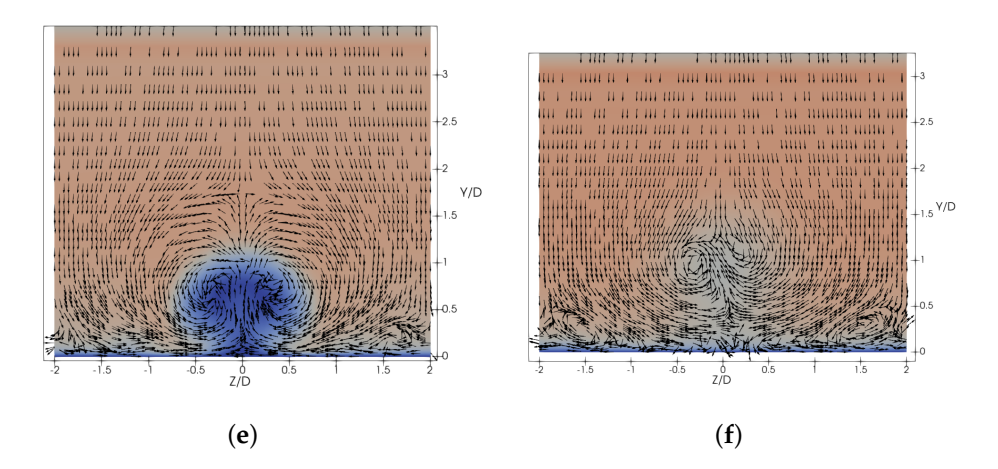


Figure 18. Iso-contours of the mean velocity magnitude with vector plots at different YZ planes, X/D = 2 and 7.5. (a) VR = 0.5 ZPG X/D = 2. (b) VR = 0.5 ZPG X/D = 7.5. (c) VR = 0.5 FPG X/D = 2. (d) VR = 0.5 FPG X/D = 7.5. (e) VR = 1 FPG X/D = 2. (f) VR = 1 FPG X/D = 7.5.

Figure 19 exhibits iso-surfaces (positive and negative values) of the time-averaged wall-normal vorticity (Ω_y [1/s]) of the three DNS cases in this study. The horseshoe vortices "encircling" the jet can be seen. As previously discussed in Figure 18, the underlying vortices at low-velocity ratios dissipate quickly; while at higher velocity ratios, the turbulent structures stay coherent for longer distances downstream of the jet. Furthermore, the presence of the counter-rotating vortex pair (CVP) is evident and both "legs" have been perfectly captured by extracting constant values of Ω_y (positive in red, negative in blue). There is an obvious damping effect of the favorable pressure gradient (FPG) on the CVP wake development for the same velocity ratio (Case 1 vs. Case 2). Far downstream of the jet and in the near-wall region, iso-surfaces of vertical vorticity show an oblong shape with a spanwise squeezed silhouette since very strong FPG induces a stretching process, particularly on low/high-speed turbulent streaks and streamwise vortices.

In Figure 20, iso-contours of the time-averaged temperature field are depicted at the X-Y plane located in the middle spanwise direction. Additionally, several streamlines have been included. For all cases, the shear-layer is observed as well as the jet trajectory. Clearly, the absence of streamwise pressure gradient (i.e., ZPG) allows a better penetration of the vertical jet into the turbulent boundary layer, as inferred from Figure 20a,b. Furthermore, in Figure 20a,b, it is seen that at a low-velocity ratio (i.e., VR = 0.5 in cases 1 and 2), the cold fluid emanating from the jet (in blue) remains close to the wall. This is crucial in film cooling since the purpose is to create a protecting layer over the surface from the hot gases in the outer part of the boundary layer. On the other hand, in the high-velocity ratio case (VR = 1), the jet possesses sufficient momentum to significantly penetrate into the turbulent boundary layer and deflect the incoming streamlines. Furthermore, the cold fluid from the jet now detaches from the surface, which would be detrimental for the thermal efficiency of the film cooling technique. However, since vertical turbulent mixing is enhanced, high-velocity ratios would be effective in combustion and chemical mixing processes. These effects have a longer-lasting impact than in the previous two cases, Case 1 and Case 2, respectively.

Taking a top view of the time-averaged temperature of the cases (Figure 21) allows us to visualize the downstream convection and diffusion of the passive scalar (temperature) introduced at the jet. The ZX plane is very close to the wall, located in the linear viscous layer. It is seen that for the low-velocity ratio, the cold fluid zone (blue) assumes an elliptical shape with a little larger streamwise dimension in Case 2. It can be inferred that flow acceleration due to FPG convects the passive scalar more effectively, as seen in Figure 21a,b. These colder flows, as compared to the incoming hot flow in red, stay longer and closer to the wall, thus having a longer protecting effect. With the high-velocity ratio

Energies **2022**, 15, 4296 21 of 30

as in Case 3, the jet intrudes more into the turbulent boundary layer, thus having less cooling effect on the surface. Furthermore, note the expansion of the cold fluid zone at the lateral regions of the jet. This effect most likely occurs due to the stronger horseshoe vortex formation.

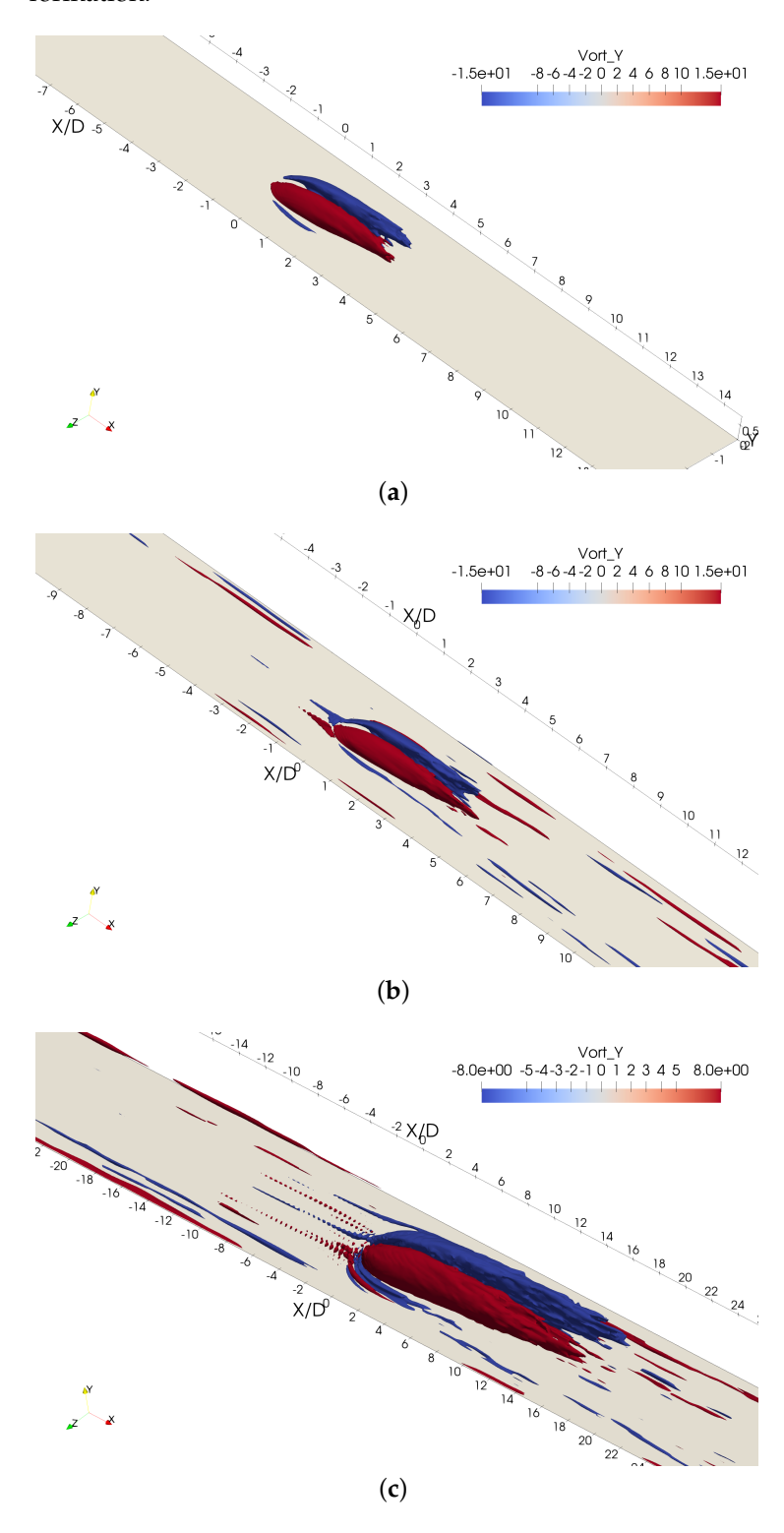


Figure 19. Iso-surfaces of time averaged wall-normal vorticity Ω_y (1/s). (a) VR = 0.5 ZPG. (b) VR = 0.5 FPG. (c) VR = 1 FPG.

Energies **2022**, 15, 4296 22 of 30

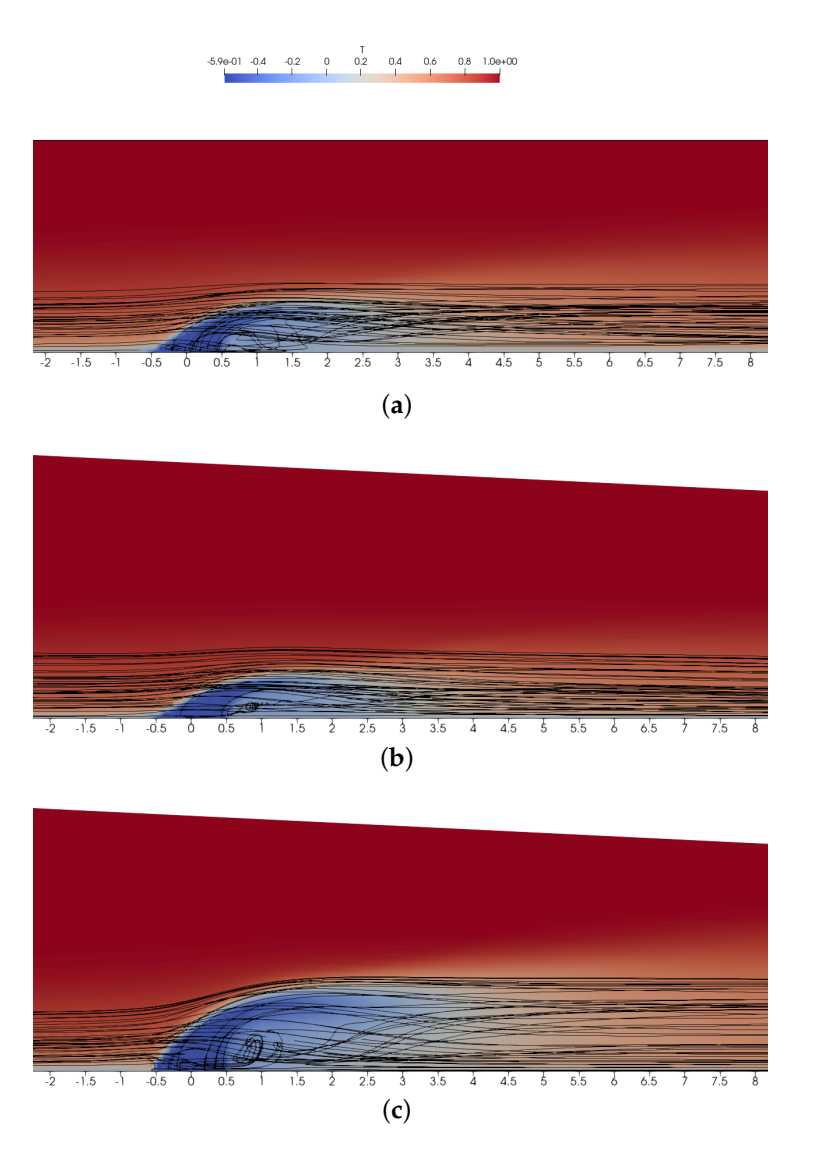


Figure 20. Iso-contours of temperature plus some streamlines in the centerline plane YX. (a) VR = 0.5 ZPG. (b) VR = 0.5 FPG. (c) VR = 1 FPG.

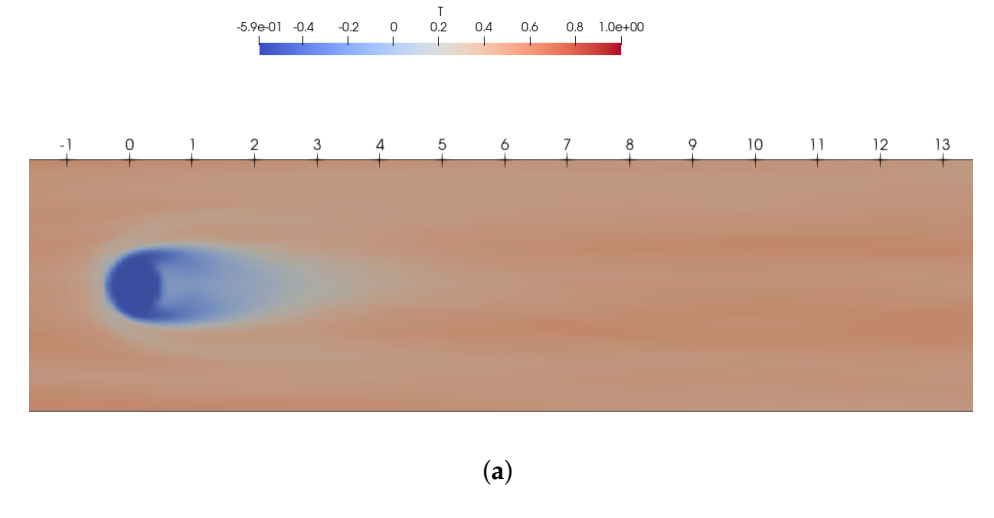


Figure 21. Cont.

Energies **2022**, 15, 4296 23 of 30

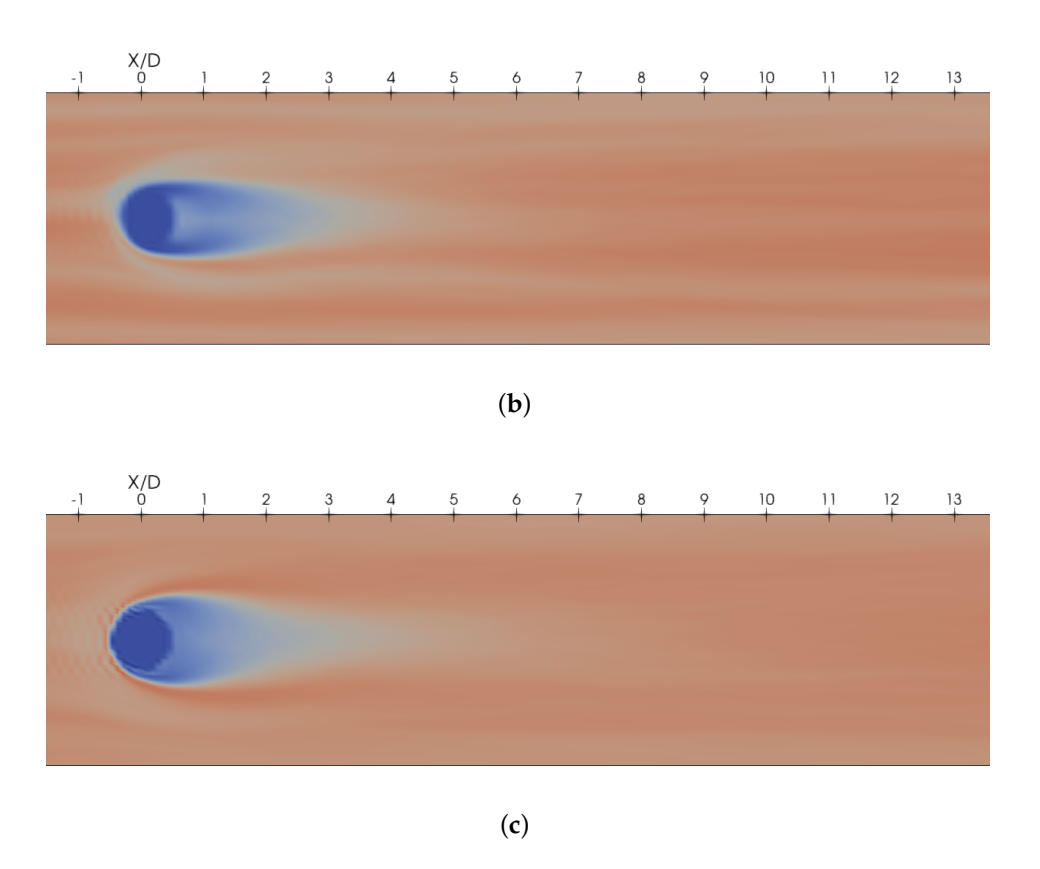


Figure 21. Topview of coolant concentration contours (passive scalar) at $y^+ \approx 0$. (a) VR = 0.5 ZPG. (b) VR = 0.5 FPG. (c) VR = 1 FPG.

Iso-surface extraction of the Turbulent Kinetic Energy (TKE) was performed and plotted in Figure 22 in order to identify and visualize the CVP structure caused by the crossflow jet. From Figure 22, it can be interpreted that in the low-velocity ratio cases (i.e., Cases 1 and 2), there are some zones with high levels of TKE downstream of the jets. Clearly, the recirculation flow zone or bubble possesses a low level of turbulent kinetic energy. The external boundaries of the CVP are dictated by high values of TKE. In Cases 1 and 2 with VR = 0.5, the TKE iso-surface zone is dissipated quickly by four diameters from the jet center. On the contrary, in the high-velocity ratio case (Case 3), not only the kinetic energy remains coherent for a longer distance downstream, but it is also present upstream of the jet. In that region, the presence of a strong APG causes turbulence enhancement. Considering the instantaneous velocity fluctuations in the streamwise (u')and in the perpendicular direction (v'), one can infer how the events in the turbulent quadrant affect the turbulent transport of momentum. The cross-correlation of u' and v' is called the Reynolds shear stress, which plays a crucial role in turbulent mixing. The extracted iso-surfaces (negative and positive) in Figure 23 show negative values of $\langle u'v' \rangle$ in the shear layer zone (top boundary of the CVP) as well as in the horseshoe vortex formation, which means that we have ejection (Q2) and sweep (Q4) events dominating these regions. The positive $\langle u'v' \rangle$ regions are attributed to backflow and boundary layer detachment (domination of Q1 and Q3 events), as previously reported in the literature. As seen in the previous Figure 23a-c, although all three cases show both positive and negative $\langle u'v' \rangle$ values, Case 3 with the high-velocity ratio has the larger influence areas where the flow remains coherent.

Energies **2022**, 15, 4296 24 of 30

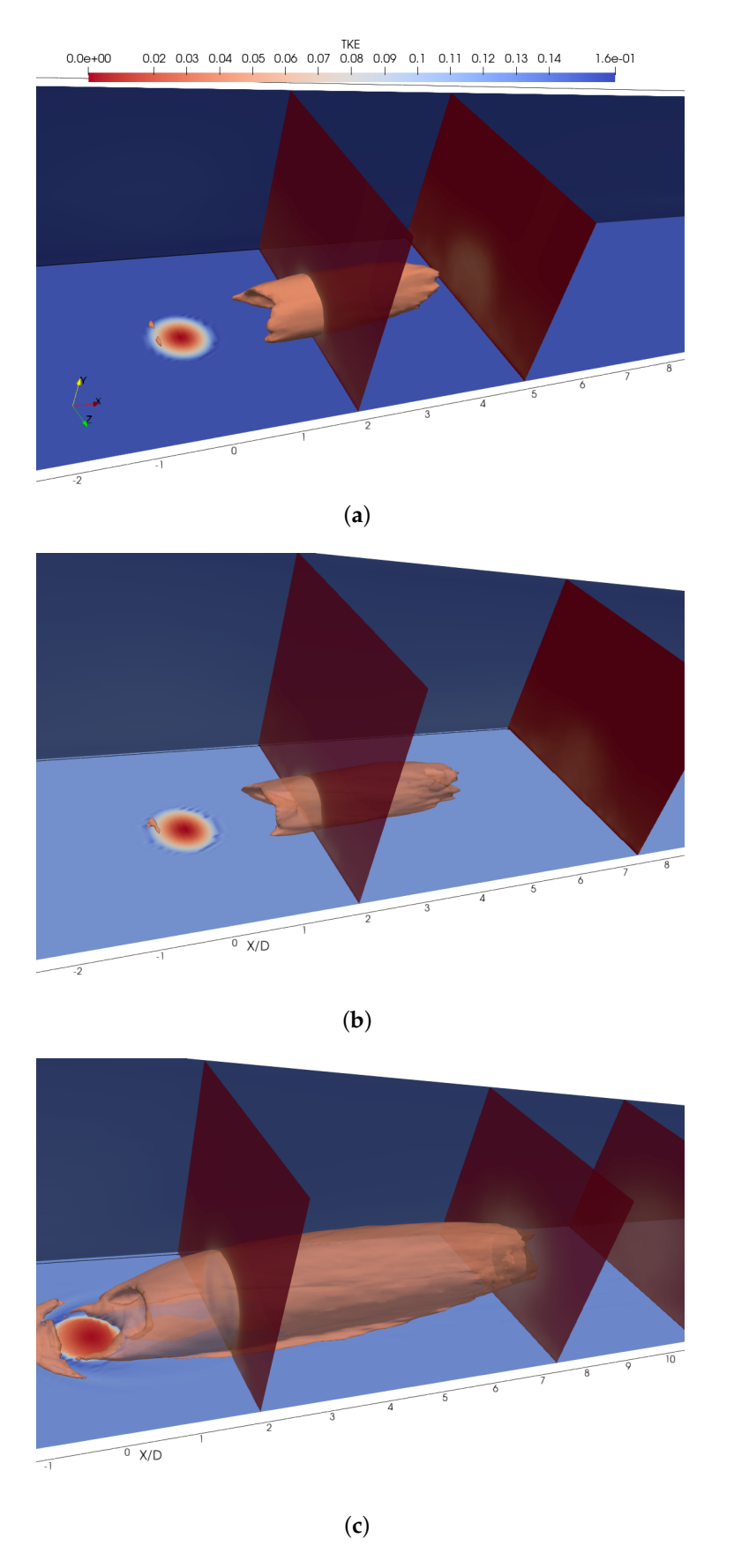


Figure 22. Iso-surfaces of TKE taken as 25% of the obtained maximum value for VR = 1. (a) VR = 0.5 ZPG. (b) VR = 0.5 FPG. (c) VR = 1 FPG.

Energies **2022**, 15, 4296 25 of 30

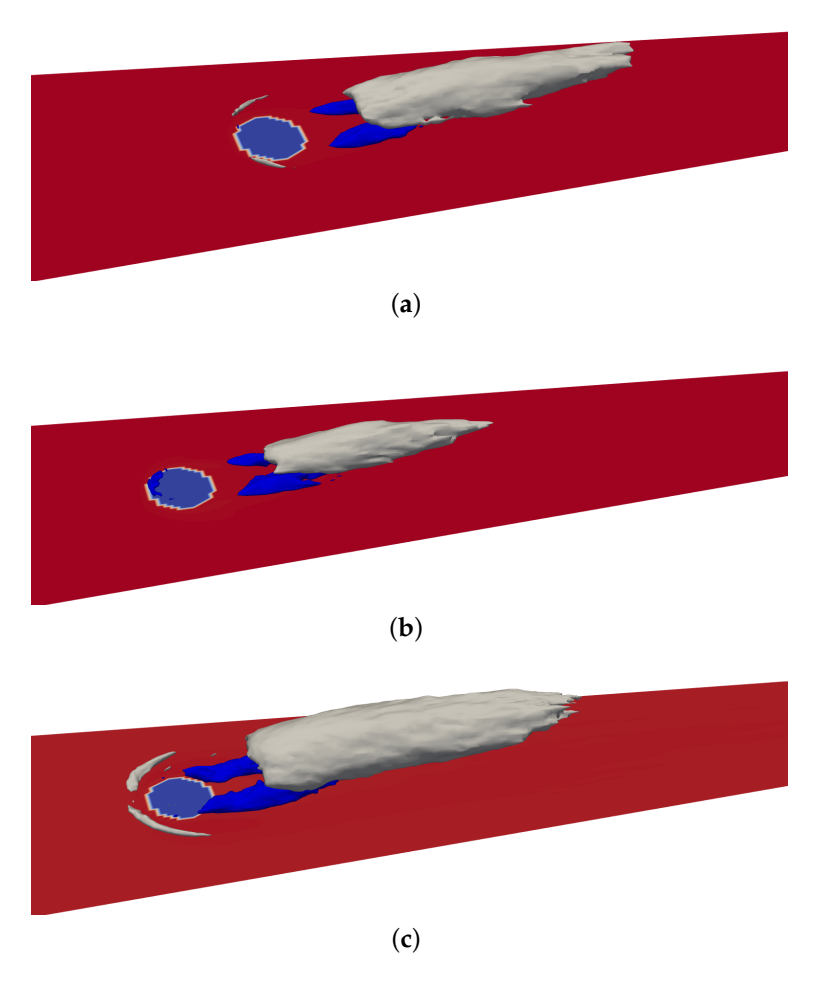


Figure 23. Iso-surfaces of positive (blue) and negative (gray) Reynolds shear stresses $\langle u'v' \rangle$ extracted as 25% of the obtained maximum value for VR = 1. (a) VR = 0.5 ZPG. (b) VR = 0.5 FPG. (c) VR = 1 FPG.

5. Conclusions

This research is based on Direct Numerical Simulation (DNS) over incompressible vertical crossflow jet problems with passive scalar transport to find out the underlying flow physics involved. In summary, the major conclusions are as follows:

- 1. A strong FPG provokes a slower recovery of the skin friction coefficient. Furthermore, there is no change in the Stanton number across the jet hole, as occurs in the skin friction coefficient, since this region is isothermal.
- The upward motion of low momentum fluid by the CVP legs encounters the downward flow from the inviscid outer region, inducing a shear layer. This layer is characterized by high levels of turbulent mixing, turbulence production, TKE and thermal fluctuations.
- 3. The formation and development of the above-mentioned shear layer are more evident at higher velocity ratios.
- 4. In Case 1 (ZPG), the mean thermal profiles showed a thick isothermal region in the flow recirculation bubble, curtailing heat transfer. The FPG cases (i.e., Cases 2 and 3) exhibited a much thinner wall-normal isothermal or flow recirculating region.
- 5. The presence of a strong, favorable pressure gradient (FPG) leads to a damping effect on the CVP wake development.
- 6. Furthermore, turbulent structures show an oblong or elongated shape with a spanwise squeezed silhouette since FPG causes a stretching process, particularly in the near-wall turbulence structures (low/high speed streaks and streamwise vortices).

Energies **2022**, 15, 4296 26 of 30

Author Contributions: Conceptualization, G.A. and C.Q.; methodology, G.A.; software, G.A. and C.Q.; validation, G.A. and C.Q.; formal analysis, G.A. and C.Q.; investigation, G.A. and C.Q.; resources, G.A.; data curation, C.Q.; writing—original draft preparation, G.A.; writing—review and editing, G.A.; visualization, G.A. and C.Q.; supervision, G.A.; project administration, G.A.; funding acquisition, G.A. All authors have read and agreed to the published version of the manuscript.

Funding: This work was supported in part by the Center for the Advancement of Wearable Technologies and the National Science Foundation under grant OIA-1849243. This material is based upon work supported by the National Science Foundation under Grant No. 1847241. This work was supported in part by a grant from the Air Force Office of Scientific Research (#FA9550-22-1-0089) and from the DoD High-Performance Computing Modernization Program (HPCMP).

Institutional Review Board Statement: Not applicable.

Informed Consent Statement: Not applicable. **Data Availability Statement:** Not applicable.

Conflicts of Interest: The authors declare no conflict of interest.

Appendix A

In this appendix, the suitability of the mesh resolution and time step is demonstrated by means of the computation of the Kolmogorov length/time and the Obukhoff-Corrsin length scales. Furthermore, the Kolmogorov length scale is defined as $\eta_k = (v^3/\epsilon)^{1/4}$, where ϵ is the average rate of energy dissipation per unit mass, and ν is the kinematic viscosity of the fluid. Moin and Mahesh [50] articulated that the smallest resolved length scale in DNS should be of the order of the Kolmogorov length scale, not lower than or equal; thus, $\Delta y < 10\eta_k$. In Table A1, we have computed η_k in the near-wall region and in the outer region of the boundary layer at x/D = 0.5 for Cases 1, 2 and 3. This streamwise location (i.e., x/D = 0.5) has been selected since maximum values of TKE dissipation were observed; thus, the smallest Kolmogorov scales should be located in that critical region. Notice that flow statistics were computed at the symmetry plane of the jet (i.e., at z/D = 0). From Table A1, it can be inferred that our DNS mesh resolution is sufficient to capture the smallest scales of the flow (e.g., $\Delta y^+ < 10\eta_k^+$) even in the high-dissipative region (or zone of very small scales) of the crossflow jet. Similarly, Table A2 depicts the Kolmogorov time scales also at three different wall distances for both cases. The Kolmogorov time scale is defined as $\tau_{\eta} = (\nu/\epsilon)^{1/2}$. In the present study, the time steps are chosen by considering the Courant, Friedrichs, Levy (CFL) parameters approximately equal to 0.36 (Case 1), 0.14 (Case 2), and 0.07 (Case 3), which results in accurate prediction of turbulence statistics. According to [51], "turbulence fluctuations can only be sustained if the computational time step is appreciably less than the Kolmogorov time scale". It can be observed from Table A2 that the selected time steps in wall units (i.e., Δt^+) are significantly lower than the corresponding dimensionless Kolmogorov time scales, τ_n^+ , at all vertical coordinates considered. Furthermore, according to [52], the smallest resolved thermal length scale in DNS should be of the order of the Obukhoff–Corrsin length scale, l_C for Pr < 1, or Batchelor scale, λ_B for $Pr \geq 1$. For the present study (Pr = 0.71), the Obukhoff–Corrsin length scale is defined as $l_C = \eta_k P r^{-3/4}$, which is larger than the Kolmogorov length scale. Therefore, by resolving the Kolmogorov length scales, the Obukhoff-Corrsin length scales should also be captured. Table A3 shows the Obukhoff-Corrsin length scales at three different wall distances for the DNS cases. One can observe that the mesh resolutions are within the order of l_C (i.e., $\Delta y^+ < 10l_C^+$). Therefore, the grid points for the current mesh are sufficient to resolve even the smallest thermal scales in the crossflow jet.

Energies 2022, 15, 4296 27 of 30

	Table A1. Ko	lmogorov i	length sca	les at x	D =	0.5.
--	--------------	------------	------------	------------	-----	------

	Cas		Case 2				Case 3				
y^+	$ \epsilon^+ $	η_k^+	Δy^+	y^+	$ \epsilon^+ $	η_k^+	Δy^+	y^+	$ \epsilon^+ $	η_k^+	Δy^+
0.035	587.5	0.2	0.035	0.042	715.3	0.19	0.042	0.072	1238	0.17	0.072
5	71.5	0.34	0.5	5	41	0.39	0.386	5	230.2	0.26	0.40
50	1.2	0.95	3.97	50	4.36	0.69	3.3	50	1.65	0.88	3.45

Table A2. Kolmogorov time scales at x/D = 0.5.

		Case 2				Case 3					
y^+	$ \epsilon^+ $	$ au_{\eta}^+$	Δt^+	y^+	$ \epsilon^+ $	$ au_{\eta}^+$	Δt^+	y^+	$ \epsilon^+ $	$ au_{\eta}^+$	Δt^+
0.035	587.5	0.041	0.013	0.042	715.3	0.037	0.0055	0.072	1238	0.028	1.13×10^{-5}
5	71.5	0.12	0.013	5	41	0.16	0.0055	5	230.2	0.066	1.13×10^{-5}
50	1.2	0.91	0.013	50	4.36	0.48	0.0055	50	1.65	0.78	1.13×10^{-5}

Table A3. Obukhoff–Corrsin length scales at x/D = 0.5.

	Cas			Cas	e 2		Case 3				
y^+	$ \epsilon^+ $	l_C^+	Δy^+	y^+	$ \epsilon^+ $	l_C^+	Δy^+	y^+	$ \epsilon^+ $	l_C^+	Δy^+
0.035	587.5	0.26	0.035	0.042	715.3		0.042		1238	0.22	0.042
5	71.5	0.44	0.5	5	41	0.5	0.386	5	230.2	0.336	0.4
50	1.2	1.22	3.97	50	4.36	0.89	3.3	50	1.65	1.14	3.45

Figure A1a shows the mean streamwise velocity profile in wall units in the ZPG region of the unperturbed ZPG-FPG case, where the local momentum thickness Reynolds number is $Re_{\theta} = 382$. A good agreement is obtained with DNS data from Skote [53] in ZPG flows at similar Reynolds numbers. In [53], the laminar-transition region was resolved in order to obtain fully turbulent statistics. The Reynolds shear stresses $\overline{u'v'}$ in present DNS are depicted by Figure A1b with a very good agreement with DNS from Skote [53], as well.

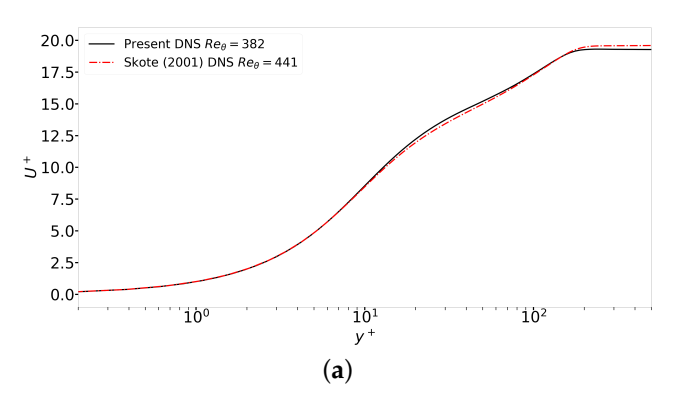


Figure A1. Cont.

Energies **2022**, 15, 4296 28 of 30

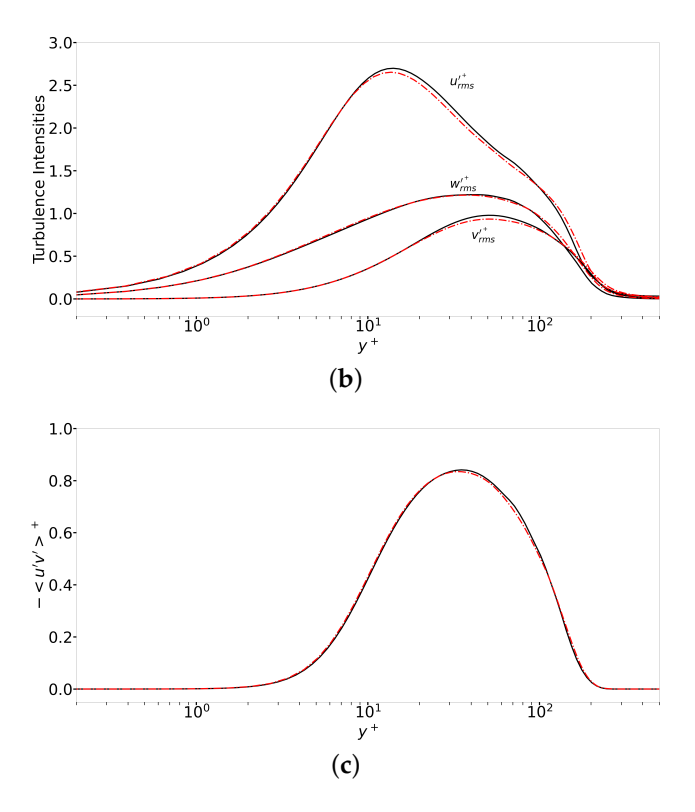


Figure A1. (a) Mean streamwise velocity, (b) turbulence intensities and (c) Reynolds shear stresses in wall units for the ZPG region (unperturbed case).

Figure A2 exhibits a comparison of present DNS with experiments by Andreopoulos [54] performed at the same velocity ratio (VR = 0.5). Profiles of $u^{\prime 2}$ (streamwise Reynolds normal stresses) at the jet centerline are shown at two streamwise locations: very close to the jet (x/D=0.5) and farther downstream (x/D=4). In general, the qualitative comparison of present DNS with experiments is fairly good. It seems that peak values of $u^{\prime 2}$ are underpredicted by our DNS; however, this may be attributed to the significantly higher value of the Reynolds number (based on the hole diameter and V_{max}) in experiments, which was approximately 14 times larger than that of present value.

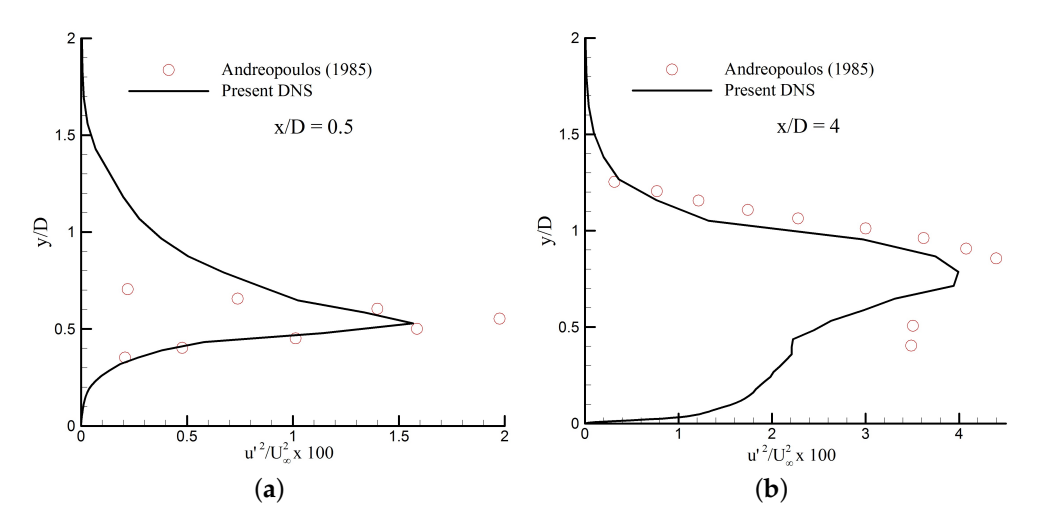


Figure A2. Profiles of streamwise Reynolds normal stresses for x/D: (a) 0.5, (b) 4.

Energies **2022**, 15, 4296 29 of 30

References

Kral, L.D. Active flow control technology. In ASME Fluids Engineering Division Newsletter; ASME: Missouri, MO, USA,1999; pp. 3–6.

- 2. Gad-el-Hak, M. Flow Control: Passive, Active, and Reactive Flow Management; Cambridge University Press: Cambridge, UK, 2000.
- 3. Greenblatt, D.; Whalen, E.; Wygnanski, I. Introduction to the flow control virtual collection. AIAA J. 2019, 57, 3111–3114.
- 4. Balakumar, B.J.; Adrian, R. Large- and very-large-scale motions in channel and boundary layer flows. *Philos. Trans. R. Soc. A* **2007**, *365*, 665–681.
- 5. Hutchins, N.; Marusic, I. Large-scale influences in near-wall turbulence. Philos. Trans. R. Soc. 2007, 365, 647–664.
- 6. Corke, T.; Thomas, F. Active and passive turbulent boundary-layer drag reduction. AIAA J. 2018, 56, 3835–3847.
- 7. Gad-El-Hak, M.; Hussain, A. Coherent structure in a turbulent boundary layer, Part 1: Generation of artificial bursts. *Phys. Fluids* **1986**, 29, 2124–2139.
- 8. Gad-El-Hak, M.; Blackwelder, R.F. Selective suction for controlling burst events in the boundary layer. AIAA J. 1989, 27, 308–314.
- 9. Fric, T.; Roshko, A. Vortical structure in the wake of a transverse jet. J. Fluid Mech. 1994, 279, 1–47.
- 10. Kelso, R.; Lim, T.; A.E., P. An experimental study of round jets in cross-flow. J. Fluid Mech. 1996, 306, 111–144.
- 11. Karagozian, A. The jet in crossflow. Phys. Fluids 2014, 26, 101303.
- 12. New, T.; Lim, T.; Luo, S. Elliptic jets in cross-flow. J. Fluid Mech. 2003, 494, 119–140.
- 13. Muldoon, F.; Acharya, S. Direct numerical simulation of pulsed jets in crossflow. Comput. Fluids 2010, 39, 1745–1773.
- 14. Sau, R.; Mahesh, K. Optimization of pulsed jets in crossflow. J. Fluid Mech. 2010, 653, 365–390.
- 15. Hansen, L.; Bons, J.P. Flow measurements of vortex-generator jets in a separating boundary layer. *J. Propuls. Power* **2006**, 22:3, 558–566.
- 16. Wernet, M.; Wroblewski, A.; Locke, R. *A Dual-Plane PIV Study of Turbulent Heat Transfer Flows*; Technical Report; NASA: Washington, DC, USA, 2016.
- Ye, L.; Liu, C.L.; Zhu, H.R.; Luo, J.X. Experimental investigation on effect of cross-flow Reynolds number on film cooling effectiveness. AIAA J. 2019, 57, 4804

 –4818.
- 18. Goldstein, R.J. Film cooling. In *Advances in Heat Transfer*; Elsevier: Amsterdam, The Netherlands, 1971; pp. 321–379, doi:10.1016/S0065-2717(08)70020-0.
- 19. Bunker, R.S. A Review of Shaped Hole Turbine Film-Cooling Technology. J. Heat Transf. 2005, 127, 441, doi:10.1115/1.1860562.
- Shyam, V.; Poinsatte, P.; Thurman, D.; Ameri, A. Long Hole Film Cooling Dataset for CFD Development—Flow and Film Effectiveness. In Proceedings of the 50th AIAA/ASME/SAE/ASEE Joint Propulsion Conference, Propulsion and Energy Forum, Cleveland, OH, USA, 28–30 July 2014; Volume AIAA 2014-3522.
- 21. Kamotani, Y.; Greber, I. Experiments on a turbulent jet in a cross flow. AIAA J. 1972, 20, 1425–1429.
- 22. Shyam, V.; Johnson, P. LES of a Film Cooling Flow Injected From an Inclined Discrete Cylindrical Hole Into a Crossflow With Zero-Pressure Gradient Turbulent Boundary Layer; Technical Report; NASA: Washington, DC, USA, 2012.
- 23. Smith, S.H.; Mungal, M.G. Mixing, structure and scaling of the jet in crossflow. J. Fluid Mech. 1998, 357, 83–122.
- 24. Bagheri, S.; Schlatter, P.; Schmid, J.P.; Henningson, D.S. Global stability of a jet in crossflow. J. Fluid Mech. 2009, 624, 33–44.
- 25. Mahesh, K. The interaction of jets with crossflow. Annu. Rev. Fluid Mech. 2013, 45, 379-407.
- 26. Muppidi, S.; Mahesh, K. Direct numerical simulation of passive scalar transport in transverse jets. J. Fluid Mech. 2008, 598, 335–360.
- 27. Liu, C.; Araya, G.; Leonardi, S. The role of vorticity in the turbulent/thermal transport of a channel flow with local blowing. *Comput. Fluids* **2017**, *158*, 133–149.
- 28. Coletti, F.; Elkins, C.J.; Eaton, J.K. An inclined jet in crossflow under the effect of streamwise pressure gradients. *Exp. Fluids* **2013**, 54, 1589.
- 29. Hutchins, N.; Marusic, I. Evidence of very long meandering features in the logarithmic region of turbulent boundary layers. *J. Fluid Mech.* **2007**, *579*, 1–28.
- 30. Araya, G.; Castillo, C.; Hussain, F. The log behaviour of the Reynolds shear stress in accelerating turbulent boundary layers. *J. Fluid Mech.* **2015**, *775*, 189–200.
- 31. Narasimha, R.; Sreenivasan, K. Relaminarization in highly accelerated turbulent boundary layers. J. Fluid Mech. 1973, 61, 417–447.
- 32. Whiting, C.H.; Jansen, K.E.; Dey, S. Hierarchical basis in stabilized finite element methods for compressible flows. *Comp. Meth. Appl. Mech. Eng.* **2003**, *192*, 5167–5185.
- 33. Jansen, K.E. A stabilized finite element method for computing turbulence. Comp. Meth. Appl. Mech. Eng. 1999, 174, 299–317.
- 34. Whiting, C.H.; Jansen, K.E. A stabilized finite element method for the incompressible Navier-Stokes equations using a hierarchical basis. *Int. J. Numer. Methods Fluids* **2001**, *35*, 93–116.
- 35. Sun, C. Parallel Algebraic Multigrid for the Pressure Poisson Equation in a Finite Element Navier-Stokes Solver. Ph.D. Dissertation, Rensselaer Polytechnic Institute, Troy, NY, USA, 2001.
- 36. Araya, G.; Castillo, L.; Meneveau, C.; Jansen, K. A dynamic multi-scale approach for turbulent inflow boundary conditions in spatially evolving flows. *J. Fluid Mech.* **2011**, *670*, 518–605.
- 37. Araya, G.; Castillo, L. DNS of turbulent thermal boundary layers subjected to adverse pressure gradients. *Phys. Fluids* **2013**, 25, 095107.
- 38. Cardillo, J.; Chen, Y.; Araya, G.; Newman, J.; Jansen, K.; Castillo, L. DNS of a turbulent boundary layer with surface roughness. *J. Fluid Mech.* **2013**, 729, 603–637.

Energies **2022**, 15, 4296 30 of 30

39. Doosttalab, A.; Araya, G.; Newman, J.; Adrian, R.; Jansen, K.; Castillo, L. Effect of small roughness elements on thermal statistics of a turbulent boundary layer at moderate Reynolds number. *J. Fluid Mech.* **2015**, *787*, 84–115.

- 40. Whiting, C.H. Stabilized finite element methods for fluid dynamics using a hierarchical basis. Ph.D. Thesis, Rensselaer Polytechnic Institute, Troy, NY, USA, 1999.
- 41. Lund, T.; Wu, X.; Squires, K. Generation of turbulent inflow data for spatially-developing boundary layer simulations. *J. Comput. Phys.* **1998**, *140*, 233–258.
- 42. Wu, X.; Moin, P. A direct numerical simulation study on the mean velocity characteristics in turbulent pipe flow. *J. Fluid Mech.* **2008**, *608*, 81–112.
- 43. Spalart, P. Numerical study of sink-flow boundary layers. J. Fluid Mech. 1986, 172, 307–328.
- 44. Kline, S.J.; Reynolds, W.C.; Schraub, F.A.; Runstadler, P.W. The structure of turbulent boundary layers. *J. Fluid Mech.* **1967**, 30, 741–773.
- 45. Patel, V. Calibration of the Preston tube and limitation on its use in pressure gradients. *J. Fluid Mech.* **1965**, 23, 185–208.
- 46. Lee, J.H.; Lee, J.; Sung, H.J. Spatial features of the wall-normal structures in a turbulent boundary layer. J. Turbul. 2011, 12, N46.
- 47. Pope, S.B. *Turbulent Flows*; Cambridge University Press: Cambridge, UK, 2000.
- 48. Cantwell, B. Organized Motion in turbulent flow. Ann. Rev. Fluid Mech 1981, 13, 457–515.
- 49. Hunt, J.C.R.; Wray, A.A.; Moin, P. Eddies, streams, and convergence zones in turbulent flows. In *Studying Turbulence Using Numerical Simulation Databases*; NASA: Washington, DC, USA, 1988; pp. 193–208.
- 50. Moin, P.; Mahesh, K. Direct numerical simulation: A tool in turbulence research. Annu. Rev. Fluid Mech. 1998, 30, 539–578.
- 51. Choi, H.; Moin, P. Effects of the computational time step on numerical solutions of turbulent flow. J. Comput. Phys. 1994, 113, 1-4.
- 52. Batchelor, G.K. Small-scale variation of convected quantities like temperature in turbulent fluid Part 1. General discussion and the case of small conductivity. *J. Fluid Mech.* **1959**, *5*, 113–133, doi:10.1017/S002211205900009X.
- 53. Skote, M. Studies of Turbulent Boundary Layer Flow through Direct Numerical Simulation. Ph.D. Dissertation, Royal Institute of Technology, Stockholm, Sweden, 2001.
- 54. Andreopoulos, J. On the structure of jets in a crossflow. J. Fluid Mech. 1985, 157, 163–197.